Chromium evidence for protracted oxygenation during the Paleoproterozoic

Kaarel Mänd*[1,2], Noah J. Planavsky[3], Susannah M. Porter[4], Leslie J. Robbins[5], Changle Wang[6,7,8], Timmu Kreitsmann[2,9], Kärt Paiste[2,10], Päärn Paiste[2], Alexander E. Romashkin[11]†, Yulia E. Deines[11], Kalle Kirsimäe[2], Aivo Lepland[2,12,13], Kurt O. Konhauser[1]

[1]*Department of Earth & Atmospheric Sciences, University of Alberta, Edmonton, Alberta, Canada.*
[2]*Department of Geology, University of Tartu, Tartu, Estonia.*
[3]*Department of Earth and Planetary Sciences, Yale University, New Haven, Connecticut, USA.*
[4]*Department of Earth Science, University of California at Santa Barbara, Santa Barbara, California 93106, USA.*
[5]*Department of Geology, University of Regina, Regina, Saskatchewan, Canada.*
[6]*Key Laboratory of Mineral Resources, Institute of Geology and Geophysics, Chinese Academy of Sciences, Beijing 100029, China.*
[7]*Institutions of Earth Science, Chinese Academy of Sciences, Beijing 100029, China*
[8]*University of Chinese Academy of Sciences, Beijing 100049, China.*
[9]*Department of Physics and Earth Sciences, Jacobs University Bremen, 28759 Bremen, Germany.*
[10]*Department of Earth and Planetary Sciences, Washington University in St. Louis, St. Louis, Missouri 63130, USA.*
[11]*Institute of Geology, Karelian Research Centre, Russian Academy of Sciences, Petrozavodsk, Russia.*
[12]*CAGE—Centre for Arctic Gas Hydrate, Environment and Climate, Department of Geosciences, UiT The Arctic University of Norway, Tromsø, Norway.*
[13]*Geological Survey of Norway (NGU), Trondheim, Norway.*

**Corresponding author. E-mail: kaarel.mand@ut.ee.*
†Deceased Feb. 16, 2021.

Abstract

It has commonly been proposed that the development of complex life—e.g., aerobic eukaryotes—coincided with atmospheric oxygenation. To test this hypothesis, we measured chromium-based oxygen proxies in a >2400-m core from the Onega Basin (NW-Russia), deposited ~2.1–2.0 billion years ago—closely preceding the first eukaryote fossils. Fractionated chromium isotopes are documented throughout the section (max. 1.63±0.10‰

δ^{53}Cr), suggesting higher and more stable oxygen levels during this interval (possibly >100 million years) than persisted for much of the billion years before or after. Significantly, unambiguous eukaryotic fossils have not been found in the Onega Basin or any contemporaneous successions. While this does not discount an increase in biological complexity during this oxic interval, our study calls into question the causative correlation between oxygenation and biological innovation. This work further highlights that while oxygenation is a necessary precursor for diverse eukaryote rich ecosystems, it need not drive eukaryogenesis or diversification.

Introduction

Free O_2 in the atmosphere, the result of oxygenic photosynthesis, shapes ecology on the global scale. Understanding Earth's oxygenation is therefore paramount to understanding the evolution and history of life. Given that O_2-dependent metabolisms are highly energetic and that atmospheric O_2 concentrations (pO_2) correlate with increased nutrient richness (*1*), high oxygen levels are often, though controversially, thought to be necessary for 'complex' (e.g., eukaryotic) life (*2*). A distinct, but related question is whether high pO_2 alone is *sufficient* for this purpose—or in other words, was oxygenation the trigger for shifts towards more complex ecosystems. In this view, removing the O_2-limitation will quickly lead to the evolution of complex traits, such as large cell sizes and multicellularity (e.g., *3*, *4*), meaning that pO_2 above all else modulated the evolution of complex life on Earth (cf. *5*, *6*). Yet, an alternative viewpoint maintains that inferred pO_2 shifts do not correspond well with the evolutionary history of complex life (e.g., *7*), with the implication that fortuitously timed biotic novelties (cf. *8*) control when groups of organisms rise to ecological dominance, essentially independent of environmental triggers (e.g., *9*).

One way to test the correspondence between pO_2 and changes in biological complexity is to examine the record of redox changes across an extended period of time in the early Proterozoic Eon, which is commonly viewed as a key interval in the emergence of eukaryotes (*10*), and then compare it with the contemporaneous fossil record. The early Proterozoic witnessed the disappearance of mass-independent sulfur isotope fractionations by ~2.5 to 2.22 billion years ago (Ga) (*11–13*), signifying the permanent oxygenation of the atmosphere (although see *14*). This change is colloquially known as the Great Oxidation Event (GOE) (*15*). The Rhyacian Period (2.3–2.05 Ga) is notable for high positive carbon isotope fractionations in marine carbonates ($\delta^{13}C_{carb}$) (*16*). As $\delta^{13}C_{carb}$ has been closely coupled to the burial of biomass and the release of O_2 accumulated in the atmosphere, this led Bekker and Holland (*17*) to hypothesize that atmospheric O_2 levels may have reached 50% of the modern in this period. This is in accordance with signals of highly elevated seawater sulfate concentrations, including the deposition of massive evaporites (e.g., *18*) and sedimentary sulfur isotope signatures (*19*), that point to a robust marine sulfate pool that is only stable in oxygenated conditions, but pO_2 remains difficult to robustly constrain.

A more recent approach has been to use the concentrations and isotopes of redox-sensitive trace metals to infer the amount of O_2 required to mobilize those elements from the crust to the oceans where they are subsequently incorporated into sedimentary rocks. However, this approach has led to conflicting results. For instance, Mänd et al. (*20*) used the concentrations of molybdenum (Mo), rhenium (Re) and uranium (U), as well as U isotopes, in marine sediments to demonstrate that highly oxidized conditions continued up to around 2 Ga. Yet, the same Orosirian Period (2.05 to 1.8 Ga), and more generally the mid-Proterozoic (2 to 0.8 Ga), is generally thought to be characterized by lower levels of oxygen, as evidenced by muted sedimentary U concentrations (*21*), absent cerium (Ce) anomalies (*22*), and reduced Mo isotope fractionations (*23–25*). In essence, different proxies present varying views of Earth's oxygenation due to their different spatial scales and sensitivities to pO_2 that, along with the fragmentary nature of studied sedimentary successions, hinder attempts to link oxygenation to preserved shifts in fossil complexity.

A continuous record of chromium isotope fractionations ($\delta^{53}Cr$) offers one way to probe the potential links between pO_2 and the development of complex life, as substantial $\delta^{53}Cr$ fractionations are inherited from continental weathering environments in direct contact with atmospheric oxygen (*26*, *27*), although see Daye et al. (*28*) and Liu et al. (*29*). Crucially, although $\delta^{53}Cr$ fractionations record mainly deoxygenated settings in the middle Proterozoic (*30–32*), with potential episodes of oxygenation (*33–35*), there is intriguingly no evidence for middle Paleoproterozoic oxygenation from Cr isotopes—when it has been commonly proposed as a high-oxygen interval based on other proxies (*18*, *19*, *24*).

Amongst the best locations to establish a long, continuous Paleoproterozoic Cr record is the Onega Basin in the Karelian Republic, Russia (*36*). This is a >3-km-thick Paleoproterozoic succession of evaporites, carbonates, and siliciclastics, including organic-rich mudstones, intercalated with mafic igneous rocks (Figure 1). In this study, we present new bulk-rock δ^{53}Cr data from a ~2400-m-thick volcano-sedimentary drill core from the Onega Basin, obtained from the Onega Parametric Hole (OPH; drilled in 2008–2009 in the southern Onega Basin at 62.1559 N, 34.4073 E; Figure 1) (*37*). The drill core intersects ~800 m of the Tulomozero Formation, ~1500 m of the Zaonega Formation, and ~500 m of the Suisari Formation. We find that substantially fractionated sedimentary δ^{53}Cr values persist throughout the Onega Basin succession, across several facies transitions. This suggests that the Onega Basin records a protracted time period—possibly more than 100 million years (Myrs)—that was host to a fundamentally stable and oxygen-rich ocean-atmosphere system providing a platform to revisit the links between oxygen and the development of complex life.

The Onega Basin

The Onega Basin succession begins with the deposition of coarse-grained siliciclastics and lava flows onto a basement of Archean granites and gneisses (*36*). These are overlain by the ~800-m-thick Tulomozero Formation made up of evaporites and dolomites (*38*). The Zaonega Formation follows as a ~1500-m-thick volcano-sedimentary package consisting of dolostones, siliciclastic turbidites, and mudstones intercalated with mafic igneous rocks (*39*). On top of that lies the ~500-m-thick Suisari Formation comprising mainly tuffs and mafic lavas/sills (*40*). The section is capped by fluvial-lacustrine siliciclastics of the Kondopoga Formation (*36*). Following deposition, the Onega Basin underwent greenschist-facies metamorphism during the ~1.89–1.79 Ga Svecofennian orogeny, which deformed the succession into a series of northwest–southeast trending folds (*36*).

This study focuses on the Tulomozero, Zaonega, and Suisari formations that constitute the middle and upper part of the Onega Basin succession. There is significant lithofacies variation in the Tulomozero Formation—in the northern part of the basin, along with the western and eastern margins, the formation consists mainly of dolostone with varying amounts of magnesite and calcium sulphate pseudomorphs, and siliciclastic layers. By contrast, the formation in the southern part of the basin, as recorded by the drill core of the Onega Parametric Hole, begins with a ~600-meters-thick halite and anhydrite-magnesite unit that grades upwards into a dolomite dominated unit. It is likely that in its present northern extent the formation was deposited in a low-energy intertidal, sabkha or playa lake environment with fluvial influences, whereas the southern part of the basin was more restricted and evaporitic, but still experienced periodic seawater influx that sustained the accumulation of hundreds of meters of evaporites (*36*). Carbonates of the Tulomozero Formation are characterized by strongly positive $\delta^{13}C_{carb}$ values, reaching as high as 18‰, that potentially reflect local amplification of a globally ^{13}C-enriched bicarbonate pool (e.g., *38*, *41*). As such, it is one of the type sections for the Lomagundi-Jatuli carbon isotope excursion (*16*). The paragenesis of halite and calcium sulfate, together with their S and Ca isotope composition, have been taken as evidence of a large marine sulfate pool, constituting >30% of modern levels (*18*, *42*).

The overlying Zaonega Formation was, in contrast, deposited in alternating shallow and deeper water conditions, possibly in a rift basin developed on a highly active continental margin (*39*). Between 35–70% of the succession is composed of mafic sills and lavas emplaced into unconsolidated sediments (*36*). The lowermost Zaonega Formation is dominated by mudstones with common dolostone interbeds which transition into deeper-water mixed mudstones, dolostones, and siliciclastic rhythmites further up section. The formation is notable for containing extremely high organic carbon content (up to 70 wt.%), the earliest known oil field (*39*, *43*), highly elevated redox-sensitive element concentrations (*20*), and one of the earliest sedimentary phosphorus enrichments (*44*). Variable and often high pyrite S isotope ratios have been interpreted as recording a diminished global marine sulfate pool (*45*) or alternatively anomalously high local sulfate demand by microorganisms (*46*, *47*). In the lower part of the Zaonega Formation, dolostones enriched in ^{13}C record the Lomagundi-Jatuli excursion (*48*), but the best-preserved carbonates of the upper Zaonega Formation have normal-marine $\delta^{13}C$ values (*49–51*). Strongly negative $\delta^{13}C$ values in carbonates and organic matter from the middle part of the Zaonega Formation were earlier thought to reflect a global negative C isotope excursion (*52*) but are now viewed as artifacts of hydrothermal de-dolomitization (*49*) and the incorporation of methanotrophic biomass (*43*).

The deposition of the Zaonega Formation was followed by the Suisari Formation. The latter signifies a slowdown of subsidence and the infilling of the basin with hundreds-of-meters-thick subaqueous mafic-to-ultramafic lavas and sills interlayered with relatively thin, tuffaceous mudstone beds (*36*).

The age of the Onega Basin remains imprecisely constrained (Figure 1a). The most robust anchor for the older age boundary is given by a Pb–Pb age of 2449 ± 1.1 million years ago (Ma) from a pluton crosscutting the Archean basement (*53*). The Tulomozero Formation is additionally constrained by an imprecise dolomite Pb–Pb age of 2090 ± 70 Ma (*54*) and by virtue of it recording the Lomagundi-Jatuli isotope excursion (along with the lowermost Zaonega Formation), which terminated in Fennoscandia at ~2060 Ma (*55*). A single zircon from a tuff layer in the lower Zaonega Formation yielded a U–Pb age of 1982 ± 4.5 Ma (*56*). A suite of cross-cutting dykes and sills in the Onega Basin succession provide younger age boundaries. A mafic sill in the Jangozero Formation, below the Tulomozero Formation, has yielded U–Pb zircon and baddeleyite ages of 1976 ± 9 Ma (*57*) and 1975.3 ± 2.8 (*56*). Zircons in dolerite and kimberlite sills in the Zaonega Formation have been U–Pb dated to 1919 ± 18 Ma (*58*), 1956 ± 5 Ma (*59*), and 1961 ± 5.1 Ma (*56*); some of these sills have peperitic contacts, implying that the sediments were still wet and unconsolidated at the time of intrusion. Gabbro sills of the Suisari Formation, interpreted as coeval to the platformal lavas, are dated 1975 ± 24 (whole-rock and clinopyroxene Sm–Nd), 1980 ± 57 Ma (leach residue, plagioclase, and clinopyroxene Pb–Pb, *57*), 1988 ± 34 Ma (whole-rock and clinopyroxene Sm–Nd), 1985 ± 57 Ma (whole-rock and plagioclase Pb–Pb), and 1969 ± 18 Ma (whole-rock, ilmenite, and ulvöspinel Re–Os, *40*). Re–Os dates on Zaonega Formation mudstones yield an age of ~2050 Ma (*60*). Finally, a sandstone in the overlying Kondopoga Formation yielded a detrital zircon Pb–Pb age of 1967 ± 3.5 Ma (*56*). In summary, while dates are imprecise, deposition of the ~2400-m-thick succession comprising the Tulomozero, Zaonega, and Suisari formations likely spanned several tens of millions and possibly over a hundred million years. Provisionally, we constrain the age of the succession between ~2.1–2.0 Ga.

Chromium as a paleoredox proxy

The utility of Cr as a paleoredox proxy is due to its contrasting solubilities in oxygen-rich and oxygen-poor environments and the distinctive isotope fractionations associated with redox transitions. Chromium occurs in igneous rocks as insoluble Cr(III), with an isotope composition of −0.12±0.10‰ δ^{53}Cr (e.g., *61*), but can be converted to soluble Cr(VI) through reactions with manganese(IV) oxides in terrestrial weathering environments (e.g., *26*). Since the main pathway for Mn(IV) oxide formation requires molecular oxygen (although see Supplementary Text and *28*, *29*), and Cr(III) oxidation with Mn(IV) oxides induces a strong positive fractionation—theoretically ~+6‰, but lower in natural environments (e.g., *27*, *62*)—the presence of fractionated Cr in aqueous environments indirectly attests to the availability of free oxygen in the atmosphere (see Supplementary Text and *63*, *64* for alternative takes). Additional Cr isotope fractionations can occur during redox reactions in rivers (e.g., *65*) and oceans (e.g., *63*, *66*), producing δ^{53}Cr values that vary between +0.3‰ and +1.6‰ in modern seawater. Such fractionated δ^{53}Cr signals can be captured by sediments that scavenge dissolved Cr, so that the presence or absence of fractionated Cr in sediments can be used to track atmospheric oxygen levels through Earth history (*26*, *27*). Similarly, since concentrations of soluble Cr(VI) in seawater scale with the generation of Mn(IV) oxides in terrestrial settings and with the abundance of oxygen-rich settings in the oceans, Cr concentration trends in anoxic sediments (which readily scavenge dissolved Cr) have also been tied to fluctuations in the extent of anoxic and euxinic seafloor area. For example, Reinhard et al. (*67*) reported a shift from ~0.017 μg g^{-1}/μg g^{-1} Cr/Ti ratios in mid-Proterozoic mudstones to ~0.05 in Neoproterozoic mudstones, corresponding to expected shifts in atmospheric oxygen levels over the Proterozoic.

Organic-rich mudstones, such as those of the Zaonega Formation, can quantitatively capture marine δ^{53}Cr due to the fast kinetics of Cr(VI) reduction in anoxic waters, as has been demonstrated in the anoxic Cariaco Basin (e.g., *68*). Carbonates, while a much less efficient sink, capture Cr with a negative fractionation in biogenic carbonates (e.g., *69*), but possibly minimal fractionation in abiogenic ones (*70*). Therefore, δ^{53}Cr values in Tulomozero Formation carbonates can be considered a minimum boundary on seawater values. Compared to mudstones and carbonates, evaporites are much less studied in terms of their Cr isotope composition. Yet, existing work on groundwater-derived evaporites in the Atacama Desert suggests that Cr was captured quantitatively in chromate salts (*71*). Likewise, the presence of bittern salts in the lower Tulomozero Formation implies cycles of almost complete seawater evaporation in the basin, which strongly support nearly quantitative capture of all seawater components. This is confirmed by element mapping of the most ^{53}Cr-enriched evaporite sample (OPH-4081, 2305.25 m depth) which shows that chromium is hosted in diffuse, likely authigenic, reddish Fe-rich phases that are disseminated throughout the dolomite-magnesite matrix (Figure 2a).

In our Onega Basin samples, bulk Cr concentrations range between 0.3 and 2283.1 μg g^{-1}, with a median of 86.1 μg g^{-1} (n = 253). Authigenic Cr abundances, expressed as Cr/Ti (*72*), range between 0.002 and 0.694 (μg g^{-1}/μg g^{-1}; Figure 3), with a median of 0.039 (n = 253). Due to different Cr drawdown affinities of different lithologies (see Methods for classification), the median Cr/Ti value in Tulomozero Formation evaporites is 0.075 (range 0.002–0.366; n = 16); in Tulomozero and Zaonega Formation carbonates, 0.040 (range 0.008–0.694; n = 93); and in mudstones throughout the succession, 0.037 (range 0.003–0.554; n = 144). Significantly fractionated δ^{53}Cr values are present throughout the entire studied section, varying between −0.43±0.03‰ and +1.64±0.10‰ δ^{53}Cr (errors are 2σ), with an average of +0.24‰ (n = 41; Figure 3). In evaporites, δ^{53}Cr ranges between −0.34 and +1.17‰ (average +0.42‰; n = 6); in dolostones, between −0.20 and +1.17‰ (average +0.20‰; n = 14); and in mudstones, from −0.43 to +1.64‰ (average +0.22‰; n = 21) (Figure 4). These values, being the highest reported so far for the Paleoproterozoic (*27*, *67*), are difficult to explain through currently known oxygen-independent processes. For instance, ligand-based Cr(III) solubilization occurs at significantly lower rates than proton-driven solubilization (*64*), UV-based Mn(II) photo-oxidation was, by the time of the middle Paleoproterozoic, hampered by the ozone layer (*29*), and Mn(IV) oxides produced through anoxygenic photosynthesis in reduced surface settings (*28*) would have been vulnerable to back-reduction prior to diffusing to subsurface Cr weathering environments (*73*). Therefore, the data most likely reflect elevated redox potentials during the deposition of the Tulomozero and Zaonega formations (see Supplementary Text for more discussion on alternatives).

Post-depositional alteration of chromium

Due to its complex geological history, secondary processes within the Onega Basin succession may have altered some geochemical signals. For example, stromatolitic carbonates in the Tulomozero Formation have undergone pervasive dolomite/magnesite recrystallization with micritic fabrics being destroyed, but most samples have retained recognizable bedding and lamination (*38*, *42*, *48*). Zaonega Formation carbonates, where dolomite is the primary phase, have in large part been secondarily de-dolomitized to calcite, with a concomitant decrease in both their δ^{18}O and δ^{13}C values, though this has primarily affected the margins of dolomite beds (*49–51*). Furthermore, there are pervasive quartz-mica veins in the mudstones of the Zaonega Formation that were emplaced due to syn-depositional hydrothermal activity triggered by the emplacement of mafic lavas and sills or during later greenschist facies metamorphism (*46*). Elemental mapping of the most ^{53}Cr-enriched mudstone sample (OPH-1572, 1112.08 m depth) shows that Cr is enriched both in C_{org}-rich laminae, as well as in microscale mica veins, suggesting some Cr mobilization into percolating fluids (Figure 2b). Finally, there was significant hydrocarbon migration in the Zaonega Formation (*43*); although Cr accumulation or fractionation through oil migration has not been studied, oils are plausible source fluids for transition metal ore formation (*74*) and mobilization into hydrocarbons is known to fractionate some transition metals (e.g., *75*).

Despite the evidence above for post-depositional fluid alteration, several factors suggest that this process cannot explain the positively fractionated δ^{53}Cr values in the Onega Basin. First, conspicuous veins, mono-mineral clusters, and altered margins of carbonate beds were carefully screened and avoided during sample selection. Second, igneous-derived Cr from hydrothermal sources is expected to host negative or crustal δ^{53}Cr ratios (*61*), and remobilization of primary Cr(III) is likely to drive residual sediment δ^{53}Cr values more negative (*65*), yet our samples have positive δ^{53}Cr values. The lack of alteration is also evident by Cr mapping—concentrations in mica veins are highest in the areas where they cross Cr-rich laminae (Figure 2b), suggesting adjacent laminae as the source of Cr. Third, wholesale Cr alteration through hydrocarbon migration is hampered by the generally short migration distances in the Zaonega Formation (centimeter-to-meter scale, *43*), and the sub-µg g^{-1} Cr concentrations in oils implies limited capacity for Cr mobilization (*76*). Finally, the evaporite section of the lower Tulomozero Formation is composed of minerals, such as halite and bittern salts, which are highly susceptible to fluid alteration. Their persistence implies that substantial fluid movement has not occurred in these rocks.

Carbonates in the Onega Basin deserve further assessment since this lithology has a high propensity for diagenetic recrystallization. Oxygen isotope values provide a means of tracking the influence of diagenetic processes, given that more pervasive diagenesis typically leads to lower δ^{18}O values (e.g., *77*, *78*). Carbonate δ^{18}O values in our Onega Basin samples range between −17.2 and −4.8‰, with an average of −11.0±2.7‰ (VPDB; n = 45; Figure S1). However, Figure 5 shows that the samples with the highest δ^{18}O values, hence being the 'least altered,' tend to have more fractionated Cr compositions than those with low δ^{18}O values, suggesting, in the standard framework, that secondary processes likely decreased, not increased δ^{53}Cr values (cf. *78*).

Another illustration that Cr geochemistry in the Onega Basin reflects primary processes is Figure 6a, which relates Cr/Ti to δ^{53}Cr in all three lithologies. That nearly all samples lie on a general positive trend suggests that δ^{53}Cr variance throughout the Onega Basin can largely be explained through the mixing of two components—an unfractionated detrital source and a fractionated seawater source (e.g., *32*)—without needing to invoke secondary overprint.

Basin controls on the dissolved chromium pool

Even if the authigenic δ^{53}Cr reflects a seawater signal, it is possible that elevated δ^{53}Cr was only a local phenomenon, and not representative of global Cr cycling. There is strong evidence for basin restriction in the Onega Basin that would allow such a scenario—evaporite mineralogy and sedimentary textures indicative of shallow deposition abound in the Tulomozero Formation (*18*, *38*). Furthermore, the sulfur and iron isotope records in the Zaonega Formation have been interpreted to reflect varying levels of restriction (*47*, *79*). In this case, distillation of the dissolved Cr pool by preferential drawdown of ^{52}Cr (i.e., Rayleigh fractionation) could have driven δ^{53}Cr more positive. Alternatively, positive values may have resulted from an anomalously positive riverine source of Cr.

However, Cr concentrations consistently reach hundreds of μg g^{-1} over the hundreds of meters of mudstone-carbonate stratigraphy in the Zaonega and Suisari formations making it unlikely that a single point source could have provided this Cr. Distillation of the Cr pool is also unlikely, as that implies a substantial diminution of the dissolved Cr—it is far more parsimonious to invoke a fractionated open marine Cr source (e.g., *20*). Conversely, in the lower Tulomozero Formation, the precipitation of bittern salts implies that seawater evaporation and Cr drawdown likely proceeded nearly to completion, again suggesting that the global marine δ^{53}Cr signal was captured. While the shallow-water upper Tulomozero Formation carbonates present the highest likelihood of δ^{53}Cr distillation, the low efficiency of Cr incorporation into carbonates (*67*) again precludes strong distillation.

Variable Cr abundances and isotope ratios attest to differences in Cr cycling and drawdown across the Onega Basin succession (Figure 3). For example, the highest Cr/Ti ratios (up to 0.353) and δ^{53}Cr values (up to 1.64‰) are consistently present in the ~1115–1108 m interval that hosts a distinctive P-rich mudstone-dolostone contact—a marker horizon within the Onega Basin (*80*). This same interval displays extremely high TOC content (up to >70 wt.%), authigenic apatite, and fossilized sulfur cycling microbial ecosystems which are interpreted as having been formed in a highly biologically productive setting with fluctuating sulfidic–suboxic redox boundaries close to sediment surface that are especially conducive to redox-sensitive metal drawdown (*20*, *44*). Additionally, since the interval was host to a degree of hydrocarbon migration (*43*), secondary Cr accumulation may have contributed to these maximum values (though as a high-temperature process, this is unlikely to have caused isotope fractionations). On the other hand, marl samples from the transition zone of the Tulomozero and Zaonega formations (between 2100–1920 m) and in the Suisari Formation (above 640 m) host unfractionated Cr (δ^{53}Cr below −0.13‰ and −0.12‰, respectively) at low authigenic concentrations (Cr/Ti below 0.065 and 0.196, respectively). In these latter cases, high levels of plagioclase (up to 53.2%), and the presence of amphibole and titanite, suggest that the sediments may have experienced substantial volcanic ash input that delivered unfractionated, igneous Cr. Since almost all samples lie on a generally positive trend between δ^{53}Cr and Cr/Ti (Figure 6a), variation in both of these parameters can be sufficiently explained through variable Cr drawdown efficiencies or detrital input, leading to differing ratios of authigenic to detrital Cr. While it remains possible that waters in the Onega Basin experienced basin-specific Cr cycling, the presence of substantial volumes of isotopically fractionated Cr demand an oxygenated ocean–atmospheric system that can host Cr(VI)-cycling.

Atmospheric–oceanic redox in the Paleoproterozoic

The Rhyacian period has been proposed as a time of elevated oxygen abundance in the middle Paleoproterozoic, potentially sandwiched between times of comparatively lower oxygen abundance (*12*, *17*). Oxygenated conditions are evidenced by evaporite mineralogy together with calcium and sulfur isotope records that indicate elevated marine sulfate levels (*18*), consistent with high redox-sensitive element concentrations and isotope ratios (*20*, *21*, *81–85*). This period of O_2 abundance was originally tied to the Lomagundi-Jatuli carbon isotope excursion through the mechanism of excess organic carbon burial (*16*, *17*), although this interpretation has become increasing challenged (e.g., *20*, *39*, *86*).

Intriguingly, the Rhyacian rock record is characterized by very minor sedimentary Cr isotope anomalies, despite this proxy being frequently cited as evidence for atmospheric oxygenation (*27*). Previous reports of positively fractionated Cr in the Paleoproterozoic do exist (Figure 7), particularly in the ~1.85 Ga Gunflint iron formation (*26*, *87*), coupled with subtly negatively fractionated Cr in the ~1.9 Ga Schreiber Beach paleosol (*88*), both consistent with Cr(VI) solubilization and transport to the oceans. However, with the exception of meteorically derived diagenetic carbonate cements in the Gunflint Formation (*87*), these fractionations barely extend beyond the crustal mean (maximum of +0.21‰), and are even surpassed by δ^{53}Cr data from the Neoarchean that are indicative of only locally oxygenated conditions in a predominantly anoxic world. Furthermore, δ^{53}Cr values of Rhyacian iron formations are even less fractionated (up to +0.03‰) (*26*). The anomalous feature of the later Paleoproterozoic δ^{53}Cr record is high positive fractionations (up to +2.34‰) in the ~1.9 Ga Flin Flon and Beaverlodge Lake paleosols (*89*, *90*), which constitute the opposite of the expected isotope effect of oxic Cr weathering and have, thus, not been linked to oxidative Cr cycling.

Collectively, these data have been used to suggest a late Paleoproterozoic to Mesoproterozoic Cr cycle highly distinct from the modern—variable atmospheric pO_2 produced, potentially in an alternating fashion, localized positively fractionated Cr runoff related to Mn(IV) oxide cycling (*87*, *88*) or negatively fractionated runoff related to ligand- or acid-based solubilization (*89*, *90*). The oceans, meanwhile, are implied to have remained predominantly anoxic, with relatively minor fractionated Cr runoff diluted within an unfractionated marine reservoir.

In contrast to this mid-Proterozoic scenario, illustrated by a general lack of correlation between Cr/Ti and δ^{53}Cr at this time (Figure 6b), our data from the ~2.1–2.0 Ga Onega Basin suggest a modern-type Cr cycle in the Rhyacian to the early Orosirian: nearly all samples follow a positive trend between Cr/Ti and δ^{53}Cr (Figure 6a) that is a telltale sign of oxidative Cr(VI) cycling coupled to Mn(II) oxidation (*32*). Whereas Fe(II) oxidation occurs at circumneutral pH at near 0 mV potential, high-potential redox reactions ($\geqslant$500 mV) are required to oxidize Mn(II) under the same conditions. Although it remains unresolved how much, and for how long, oxygen levels would have to rise above ~0.1–1% of the present atmospheric level (PAL), as is required for substantial Mn(IV)-driven Cr(III) oxidation without quantitative Cr(VI) back-reduction by Fe(II) phases (*91*), highly fractionated δ^{53}Cr values coupled to high authigenic Cr enrichments imply globally elevated pO_2 levels (see discussion on alternative Mn oxidation and Cr fractionation mechanisms in Supplementary Text). This Cr(VI) then accumulated in predominantly oxic oceans, where the oxyanion was stable. The large, positively fractionated marine Cr pool was then further subjected to biochemical Cr redox cycling in the photic zone (e.g., *66*).

Our key finding is that the fractionated δ^{53}Cr values persist for nearly the entirety of the ~2400-m-thick sampled succession, across facies that transition from a shallow evaporative setting to a deeper water turbidite system, and most likely representing several tens to potentially more than a hundred Myrs of time (Figure 3, 7). Most parsimoniously, the data suggest that Earth's atmospheric oxygenation remained above the ~0.1–1% pO_2 threshold for Cr(III) oxidation and transport to the oceans (*91*) for the entirety of this time period. These findings provide a striking contrast to what are increasingly seen as highly variable mid-Proterozoic redox conditions (e.g., *91*, *92*). In this light, the Orosirian period perhaps witnessed a momentous transition from a well-buffered to a poorly-buffered atmospheric–oceanic redox state.

Implications for the evolution of biological complexity

Payne et al. (*3*) argued that based on the then-available fossil and pO_2 proxy evidence, the maximum body size of fossil organisms increased in two discrete steps corresponding to increases in pO_2, supporting the popular belief that elevated pO_2 is both a necessary and sufficient precondition for the evolution and radiation of complex life (*2*). Conceptually, this agrees with arguments that higher pO_2 results in generally higher nutrient richness in marine ecosystems leading to more complex ecosystem structure (*1*, *93*). Furthermore, some studies of Proterozoic fossil locales have shown that higher redox potentials are correlated with the occurrence of multicellular eukaryotes (*4*) or biomineralizing animals (*94*).

Our study provides us with an opportunity to revisit the link between pO_2 and increases in biological complexity by juxtaposing the present fossil record with the long-term record of Paleoproterozoic oxygenation revealed here (tens to more than a hundred Myrs). Complex life—of which eukaryotes may be only one example, and the only one that happened to survive to the present—is difficult to measure or even define, but typical proxies, based on our understanding of modern organisms, include large cell size (e.g., cells >100 μm), excystment structures, ornamented walls and spines, as well as incipient multicellularity (e.g., *10*, *95–97*). These features appear by ~1.65–1.5 Ga in diverse fossil assemblages in North China, India, Australia and Siberia (e.g., *98–103*) and represent a significant change from earlier assemblages displaying much less complex morphologies (*10*). These late Paleoproterozoic to early Mesoproterozoic fossils are taken to represent the oldest recognizable eukaryotic fossils, and as such provide a minimum age constraint on the origin of Total Group Eukarya (i.e., all stem and crown group eukaryotes, beginning with the first eukaryotic common ancestor), which could have appeared hundreds of millions of years earlier (*9*).

It is notable that the first appearance of complex morphologies in the fossil record occurs much later than the protracted Paleoproterozoic period of high pO_2 identified in the

Onega Basin sedimentary succession, instead taking place during a period commonly described as deficient in O_2 (*104*). In fact, since the collection of the OPH core in 2009, as well as the FAR-DEEP drill cores in 2007 (1900 m of core in the Tulomozero and Zaonega formations, *105*), and the OnZaP drill cores in 2012 (180 m of core in the Zaonega Formation, *46*), analyses of >100 thin sections of the Onega Basin have failed to find any evidence for fossils of a similar grade of complexity often seen in the Mesoproterozoic. Indeed, the only potential finds so far observed have come from gray siltstones in the overlying Kondopoga Formation (Figure 1a), representing a later stage of basin development: acritarchs of hundreds of μm in diameter, but displaying no wall ornamentation (*106*). Similarly, no fossils showing complex morphologies have been identified from any other contemporaneous rock successions (though see discussion on Franceville Group below).

There may be several reasons for the lack of a visible increase in biological complexity during deposition of the Onega Basin strata. First, taphonomic conditions in the Onega Basin may not have been suitable for the preservation of such fossils—the high TOC levels present throughout much of the succession have been shown to anti-correlate with fossil preservation potential (*107*). Fossil preservation may also have been affected by greenschist facies metamorphism in the Onega basin (*39*). However, these arguments are unsatisfying since a diversity of well-preserved organic-walled microfossils have been found in younger greenschist-facies rocks (e.g., *108* and references therein) and in addition to high-TOC mudstones, the Onega Basin includes a large variety of sedimentary environments including some low-TOC shales and marls that are commonly fossiliferous in younger Proterozoic successions (e.g., *101*). Nor are complex fossil assemblages in this sense preserved in any other succession prior to ~1.65 Ga, in contrast with the post-1.65 Ga period in the latest Paleoproterozoic and Mesoproterozoic, though this could partly be attributed to a relative lack of paleontological work in the former interval. In any case, a further possibility is that the types of organisms which left fossils of a complexity common to the Mesoproterozoic had not yet evolved. This is not to suggest that morphologically complex organisms such as eukaryotes could not have arisen as a response to high pO_2 by ~2 Ga; it is possible they were present but did not form preservable structures. However, it is fair to argue that the best paleontological records today do not support a direct linkage between high pO_2 in the Paleoproterozoic and an observable increase in morphological complexity. Oxygen may have been necessary, but was not sufficient for this change (as argued previously by *7*, among others). In fact, the most straightforward interpretation of the data so far seems to suggest that the increase in biological complexity as recorded by the fossil record occurred at a time of low and variable pO_2 levels (*91*).

It should be noted that the above discussion hinges on the fossil record as it is currently interpreted. As a counterexample, the ~2.1 Ga Franceville Group, Gabon, hosts a differentiated assemblage of macroscopic pyritic structures as well as non-pyritized macroscopic discs and rounded aggregates interpreted to be the remains of complex macroscopic organisms (*109*, *110*), and fungus-like filamentous structures have been described from basalt vesicles in the ~2.4 Ga Ongeluk Formation, South Africa (*111*). Similarly, pyritized strong-shaped structures in shales from the Franceville Group (*112*) and U-shaped ridges in sandstones from the 2.0–1.8 Ga Stirling Range Formation, Australia, have been interpreted as the traces of macroscopic motile organisms (*113*), which were possibly unicellular (*114*). However, even the biogenicity of these structures is in question (e.g., *115*, *116*). If they, nevertheless, represent early eukaryotes or other forms of complex life, their absence from the Onega Basin suggests that such evolution was highly localized or that other factors facilitated their preservation only in the above-mentioned settings. Furthermore, the time of deposition in the Onega basin could have corresponded to the earliest period of eukaryote evolution, i.e. shortly after the divergence between eukaryotes and their closest living relatives (cf. *9*). Thus, although there is no obvious evidence for a jump in morphological complexity, it remains possible that cellular complexity did increase during this interval of consistently high oxygenation. Potentially, this may even have been the time that the mitochondria—which are well adapted to oxic environments—were acquired early in stem group eukaryote evolution.

Ultimately, the Proterozoic fossil record, especially in the middle Paleoproterozoic time slice, is incompletely studied. In order to identify possible causative relationships between biological innovation and oxygenation, more focused paleontological work in rocks dating from the middle Paleoproterozoic period is required.

Materials and methods

Drill core

Drill core samples were obtained from the ~3500-m-long Onega Parametric Hole (OPH), drilled in 2008–2009 in the southern Onega Basin (62.1559 N, 34.4073 E; Figure 1) (*37*). The drill core intersects ~800 m of the Tulomozero Formation, ~1500 m of the Zaonega Formation, and ~500 m of the Suisari Formation. Samples for this study were obtained from all of the aforementioned formations and constitute three sample sets: “NGU” (140 samples), “ACME” (40 samples), and “Yale” (73 samples). Care was taken to remove any macroscopically visible veins or monocrystalline mineral grains from rock slabs, especially for the “Yale” samples from which Cr isotope compositions were measured.

X-ray diffraction

The mineralogical composition of 147 samples was studied using X-ray diffractometry (XRD) at the University of Tartu, Estonia. Rock samples were ground to a fine powder, pressed into un-oriented tablets and scanned on a Bruker D8 Advance diffractometer, where a copper Kα X-ray source and a LynxEye positive sensitive detector were used to generate diffractograms in a 2–70° 2Θ range. Quantitative mineral abundances were modeled using the Rietveld algorithm-based Topaz software suite. The relative error for major mineral components (>5 wt.%) was ~10% and ~20% for minor mineral components (<5 wt.%).

Based on the results, the samples were divided into three main lithotypes: (1) evaporites (containing >10 wt.% halite, magnesite, and/or anhydrite) which mainly occur below 2330 m depth; (2) carbonates (containing >50 wt.% dolomite, calcite, magnesite, and/or siderite) above 2330 m depth that are dominated by dolomite and magnesite in the Tulomozero Formation, and dolomite-calcite in the Zaonega Formation; and (3) mudstones which first appear above 2330 m, but become dominant in the Zaonega Formation, where they contain mostly quartz, feldspars, micas and chlorite. See Supplementary Text for a more detailed description. For some mudstone and carbonate samples, mineralogical data was not available. For classification, the carbonate content of these samples was, instead, estimated using elemental abundances and the formula (Ca + Mg) / (Si + Al), with values >0.5 being considered carbonates.

Element abundances

Total organic carbon (TOC) content was measured at the Geological Survey of Norway (NGU) using a LECO SC-444 analyser ("NGU" samples) (*80*) and at the University of Alberta via loss on ignition ("ACME" and "Yale" samples). Sample aliquots weighing between 0.5 and 2 g were loaded into ceramic beakers and combusted at 500 °C for 8–12 h, and the change in mass was recorded. Element concentrations for sample set "NGU" were determined at NGU with a Philips PW 1480 X-ray fluorescence spectrometer equipped with a rhodium X-ray tube. For major elements, 0.6 g of powdered sample aliquots and 4.2 g of $Li_2B_4O_7$ were heated to 1000°C and fused into a bead using a CLAISSE FLUXER-BIS. For minor elements, samples were prepared by mixing 9.6 g of powdered sample with 2.4 g of Hoechst wax in a Spex Mixer/Mill and pressing them into a pellet using a Herzog press. The detection limits for major elements were generally below 0.02% and the typical precision (1σ) was ~2%. For minor elements, detection limits were ≤10 $\mu g\ g^{-1}$. Calibration of the XRF was done using a set of ~120 internationally certified natural rock standards as well as ~20 artificial standards provided by the XRF manufacturer.

Element concentrations for sample set "ACME" were determined at ACME Laboratories, Bureau Veritas Commodities Canada Ltd. The samples were powdered and then heated to mineralize organic carbon. Major elements were analyzed via inductively coupled plasma optical emission spectroscopy (ICP-OES) from aliquots fused into a $LiBO_2$ bead. Minor elements were digested using a mix of HNO_3, $HClO_4$, and HF and analyzed via inductively coupled plasma mass spectrometry (ICP-MS). Average relative standard deviation was less than 5% for all elements; accuracy was monitored using the OREAS 25a and OREAS 45e reference materials.

Element concentrations of sample set "Yale" were measured at the Yale Metal Geochemistry Center (YMGC). The samples were pulverized in an agate mill, combusted in ceramic crucibles at 500°C for 8h to remove organic carbon and digested in a class ten Pico-trace clean laboratory using a succession of concentrated, Teflon-distilled acids. Digestions were initiated with the addition of 3 ml of HNO_3 and 1 ml of HF, then heated at 100 °C for 24h in closed Teflon vials, before being evaporated to dryness. Once dry, 3 ml HCl and 1 ml of HNO_3 were added to each sample, and samples were heated at 95 °C for 24h before being dried down. Final residues were then taken up in 5 mL of 3N HNO_3 solution at 70°C for 1h. Prior to analyses by ICP-MS, samples were diluted 200:1 in 5% Teflon-distilled HNO_3 spiked with 1 ng g^{-1} indium (In). All samples were measured on a Thermo Scientific Element XR high-resolution ICP-MS. The In spike was used to correct for instrumental drift over the analytical session. Five dilutions of a customized internal laboratory standard were measured at the end and beginning of the analyses and several times throughout the run. Repeat analysis on the laboratory standard yielded a relative standard deviation (1σ) for all elements (excepting Na) of ≤8%, averaging ~4% across the analytical session. External accuracy was assessed by measuring the geostandard BHVO-2; relative difference between measured and known values for all elements was 8.3% on average and generally below 10%. Particularly, the Cr and Ti values for BHVO-2 were within the 95% confidence interval for accepted values (*117*). For all sample sets, Cr was normalized to the detrital tracer element titanium to assess authigenic enrichments, as suggested by Cole et al. (*72*).

Isotope ratios

Oxygen isotope ratios of carbonates from micro-drilled samples were measured at the University of Tartu using a Thermo Scientific Delta V Advantage continuous flow isotope ratio mass spectrometer and include data published in Kreitsmann et al. (*50*). The precision of the measurements was 0.2‰ (2σ) and the long-term reproducibility exceeded ±0.2‰ (2σ). The compositions are expressed as the ratio of ^{18}O over ^{16}O, normalized to the Vienna Pee Dee Belemnite (VPDB) reference standard as $\delta^{18}O$:

$$\delta^{18}O = [(^{18}O/^{16}O)_{\text{sample}} / (^{18}O/^{16}O)_{\text{VPDB}} - 1] \times 1000‰ \quad (1)$$

A correction was applied for the differing phosphoric acid fractionation factor of dolomite and calcite (*118*) according to the mineralogy of individual samples. Oxygen isotope compositions of bulk samples are presented here as an average of several micro-drilled sub-samples (1–7 micro-drilled measurements per bulk sample).

Chromium isotope compositions were determined for the “Yale” sample set at the YMGC from solutions prepared for elemental concentration analysis (see above). Sample preparation adapted the methods of Schoenberg et al. (*61*) and Reinhard et al. (*68*). An aliquot of each sample, containing ~200 ng of Cr, was diluted in 2 ml of 6N HCl and a ^{50}Cr–^{54}Cr double spike was added at a spike/sample ratio of ~0.5, in order to correct for isotope fractionation during sample processing and measurement (*61*). The samples were purified chromatographically to remove mass interference from ^{54}Fe, ^{50}Ti, and ^{50}V. First, samples were passed through columns containing AG1-X8 anionic resin, where the matrix was eluted by addition of 0.2N HCl and Cr was subsequently collected with 2N HNO_3. Second, samples were loaded on microcolumns filled with AG1-X8 resin to remove all remaining Fe, and Cr was eluted with 6N HCl. In the final step, Ti was removed using the cationic resin AG50W-X8: the matrix was eluted with 0.5N HNO_3, 0.5N HF, and 1N HCl and Cr was subsequently released with 1.8N HCl. Residues were taken up in 5% HNO_3 and analyzed on a Thermo-Finnigan Neptune Plus multicollector ICP-MS. To correct for remaining interferences, the samples were run in high-resolution mode and Fe, Ti, and V were monitored. Standard-sample bracketing with the NIST SRM 979 reference standard was employed to correct for instrumental drift. Instrumental mass bias and fractionation during sample preparation was corrected for using the Cr double-spike through the data reduction model of Siebert et al. (*119*). The Cr isotope compositions are normalized to the composition of the reference material NIST SRM 979, and reported as:

$$\delta^{53}Cr = [(^{53}Cr/^{52}Cr)_{sample} / (^{53}Cr/^{52}Cr)_{SRM979} - 1] \times 1000‰ \qquad (2)$$

The internal precision was calculated based on 20 duplicate analyses of NIST SRM 979 and reported as 2σ uncertainty. Geostandards BHVO-2B and Nod-1-a were used to monitor the external precision; the measured values were between −0.13‰ to −0.10‰ and 0.04‰ to 0.09‰, respectively, which are within error of previously reported measurements (*30*).

In-situ element mapping

In-situ element mapping of two polished samples (OPH-1572 and OPH-4081) from representative lithologies was conducted at the University of Tartu. Mapping involved parallel laser scans perpendicular to bedding from areas containing secondary silicate veins and anhydrite. Scans were performed with a Cetac LSX-213 G2+ laser system with a HelEx II fast-washout two-volume large-format cell using 800 ml min^{-1} helium as carrier gas. A square 65 µm laser spot moving left-to-right at 65 µm s^{-1} at 10 Hz and a power of 3.45 J cm^{-2} was used. The total duty cycle was 0.2 s. For sample OPH-4081, ^{24}Mg, ^{27}Al, ^{28}Si, ^{31}P, ^{34}S, ^{39}K, ^{43}Ca, ^{49}Ti, ^{51}V, ^{52}Cr, ^{55}Mn, ^{56}Fe, ^{60}Ni, ^{63}Cu, ^{66}Zn, ^{88}Sr, ^{89}Y, ^{137}Ba, ^{140}Ce, and ^{238}U were measured at a dwell time of 7 ms. For sample OPH-1572, ^{13}C, ^{27}Al, ^{28}Si, ^{31}P, ^{34}S, ^{43}Ca, ^{47}Ti, ^{51}V, ^{52}Cr, ^{55}Mn, ^{56}Fe, ^{60}Ni, ^{63}Cu, ^{66}Zn, ^{95}Mo, ^{140}Ce, and ^{238}U were measured at a dwell time of 8 ms. The composition of the volatilized material was analyzed using an Agilent 8800 quadrupole ICP-MS in single quad mode. Maps are presented as relative abundances in counts per second.

Acknowledgments

We would like to thank Roger Buick, Nicholas J. Butterfield, and Emmanuelle J. Javaux for discussions that significantly improved the manuscript.

Funding:

Ministry of Education and Research of Estonia, The Kristjan Jaak Scholarship program (KM)

UAlberta North, Ashley & Janet Cameron Graduate Scholarship (KM)

Estonian Research Council grant PRG447 (KM, TK, KK)

Natural Sciences and Engineering Research Council of Canada Discovery grant RGPIN-165831 (KOK)

European Union’s Horizon 2020 Research and Innovation Programme, Marie Skłodowska-Curie grant agreement No 894831 (KP)

Author contributions:

Conceptualization: KM, NJP, SMP, KK, AL, KOK

Methodology: NJP, PP, KK

Validation: NJP, SMP, LJR, CW, TK, KP, PP, KK, AL, KOK

Formal analysis: KM, LJR, CW, PP, KK

Investigation: KM, NJP, LJR, CW, TK, KP, PP, AER, YED, KK, AL, KOK

Resources: NJP, AER, YED, KK, AL, KOK

Writing—original draft: KM, SMP, KOK

Writing—review & editing: NJP, SMP, LJR, CW, TK, KP, PP, YED, KK, AL, KOK

Figure captions

Figure 1: Onega Basin geology. (a) Simplified stratigraphy of the Onega Basin sedimentary succession showing formation boundaries, age constraints (explained in text; superscripts are reference numbers), predominant geological features, and the location of the Onega Parametric Hole (OPH, indicated with a triangle). Modified from Melezhik et al. (*48*) and Paiste (*46*). (b) The exposures of the Tulomozero, Zaonega, and Suisari formations within the Onega Basin, NW Russia are shown by color. (c) Mafic pillow lavas of the Suisari Formation. Hammer head is ~15 cm across (outcrop on the western shore of Lake Onega, *36*). (d-i) Polished drill core photographs of common rock types of the Tulomozero and Zaonega formations. Scale bars are 1 cm across. (d) Laminated fine-grained dolostone in the upper Zaonega Formation (OnZaP drill cores, northern Onega Basin, 13 m, *46*). (e) Laminated organic- and sulphide-rich mudstone in the upper Zaonega Formation displaying soft-sediment deformation as well as quartz-mica and pyrobitumen veining (OnZaP, 63 m, *46*). (f) Rhythmically bedded greywacke-siltstone in the lower Zaonega Formation (FAR-DEEP 12AB drill core, northern Onega Basin, 282 m, *120*). (g) Pale pink dolostone of the upper Tulomozero formation with red-brown stromatolitic laminae (FAR-DEEP 11A drill core, northern Onega Basin, 107 m, *121*). (h) Massive, coarse-crystalline anhydrite in the middle Tulomozero Formation (OPH, 2510 m, *48*). (i) Brown and pink, massive, coarse-grained halite of the lower Tulomozero Formation with inclusions of anhydrite (white), magnesite (yellow), and shale (pale grey) (OPH, 2902 m, *48*).

Figure 2: In-situ element maps for representative Onega Basin samples. Optical micrographs and relative carbon, aluminum, iron, and chromium abundance maps (reported in counts per second) were determined through laser-ablation mass-spectrometry from representative lithologies in the OPH core. (a) Evaporitic carbonate sample OPH-4081 (depth 2305.25 m, δ^{53}Cr = 1.16±0.08‰), composed mainly of dolomite–magnesite, hosts disseminated Fe-rich phases, in which Cr is preferentially concentrated. (b) C_{org}-rich mudstone sample OPH-1572 (depth 1112.08 m, δ^{53}Cr 1.63±0.11‰) displays C_{org}-rich sedimentary laminae and Al-rich cross-cutting mica veins. Cr is concentrated both in the laminae and veins. Scale bars are 1 mm. Note difference in color scale.

Figure 3: Chromium geochemistry in the Onega Parametric Hole drill core. Columns show the lithology, abundance of authigenic chromium (Cr/Ti), and its isotope composition (δ^{53}Cr). Color of datapoints corresponds to lithology. Crustal averages, vertical grey bars, are taken from Cole et al. (*72*) and Schoenberg et al. (*61*).

Figure 4: Chromium isotope ratios per lithology. Boxplots show medians, 25/75th quantiles, and the full range; superimposed black circles are individual samples. Grey bar denotes average crustal composition from Schoenberg et al. (*61*).

Figure 5: Relationships between chromium and oxygen isotope ratios in carbonates. Chromium isotope ratios (δ^{53}Cr) are plotted against oxygen isotope ratios (δ^{18}O VPDB); in the latter case, lower values are indicative of stronger alteration of carbonates. Grey bar denotes average crustal composition from Schoenberg et al. (*61*).

Figure 6: Authigenic chromium abundances (Cr/Ti) plotted against isotope ratios (δ^{53}Cr). (a) Onega Basin data from this study, coloured per lithology. (b) Published data from mid-Proterozoic sections of various lithologies, coloured according to age (1950–1000 Ma). A positive trend, as opposed to a horizontal one, suggests Cr(VI) cycling and the presence of atmospheric oxygen (e.g., *32*). Data for panel b is from Frei and Polat (*88*), Planavsky et al. (*32*), Cole et al. (*30*), Gilleaudeau et al. (*34*), Canfield et al. (*33*), and Wei et al. (*35*).

Figure 7: Authigenic chromium abundances (using Cr/Ti as proxy) in shales (a) and δ^{53}Cr values in various geological archives (b) through time. Differently coloured pastel dots represent previously published data of different lithological affinities. Saturated cross symbols are data from this study. Cr/Ti data is from Reinhard et al. (*67*) and Robbins et al. (*85*); δ^{53}Cr data is from the compilation of Wei et al. (*27*) and Wei et al. (*35*). Since Cr concentrations in the crust have decreased through geological time due to a decreasing prevalence of Cr-rich ultramafic igneous rocks, samples have been normalized to changes in crustal abundance according to Condie (*122*). Grey bars represent average crustal compositions as in Figure 2.

Figures

Figure 1:

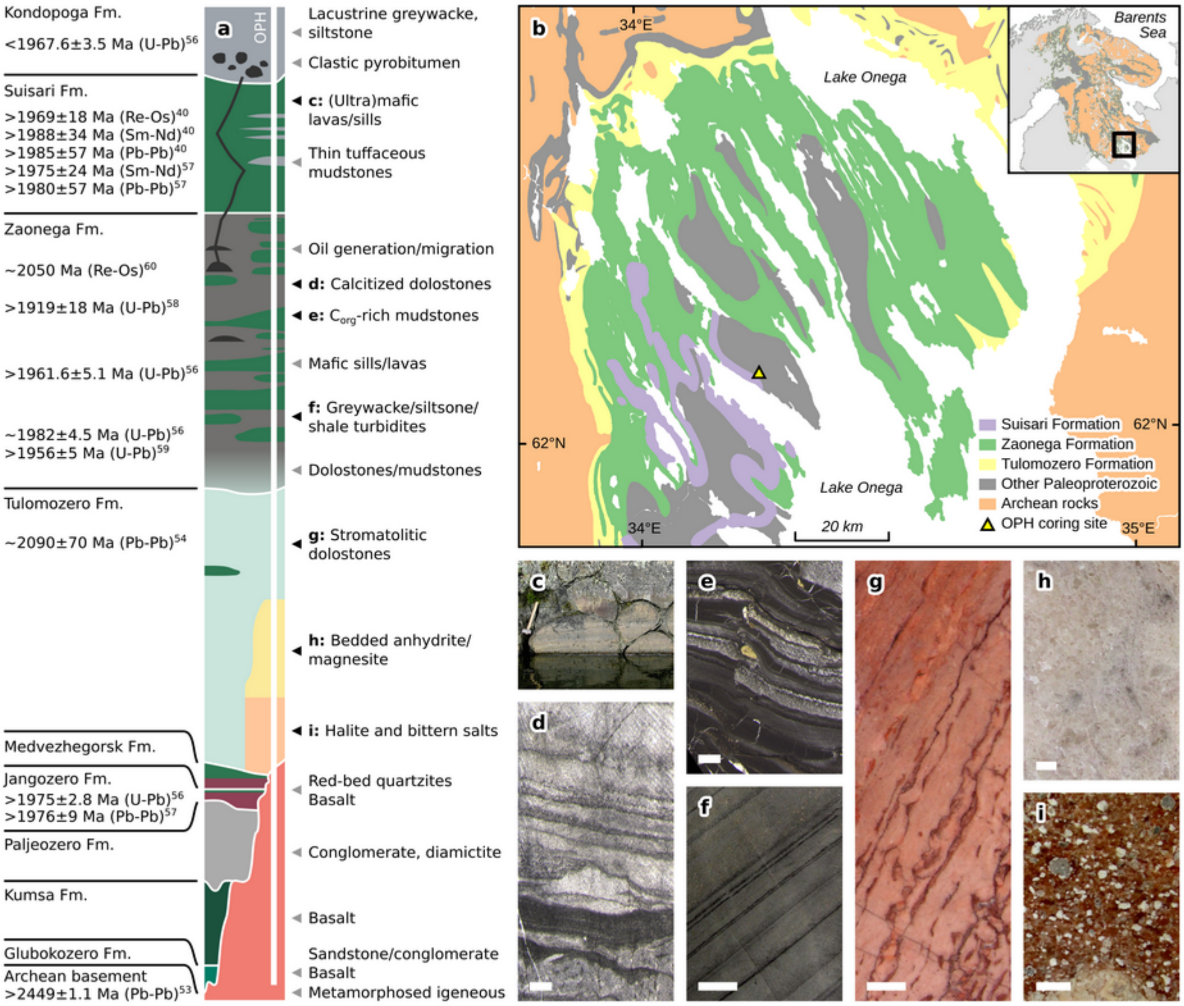

Figure 2:

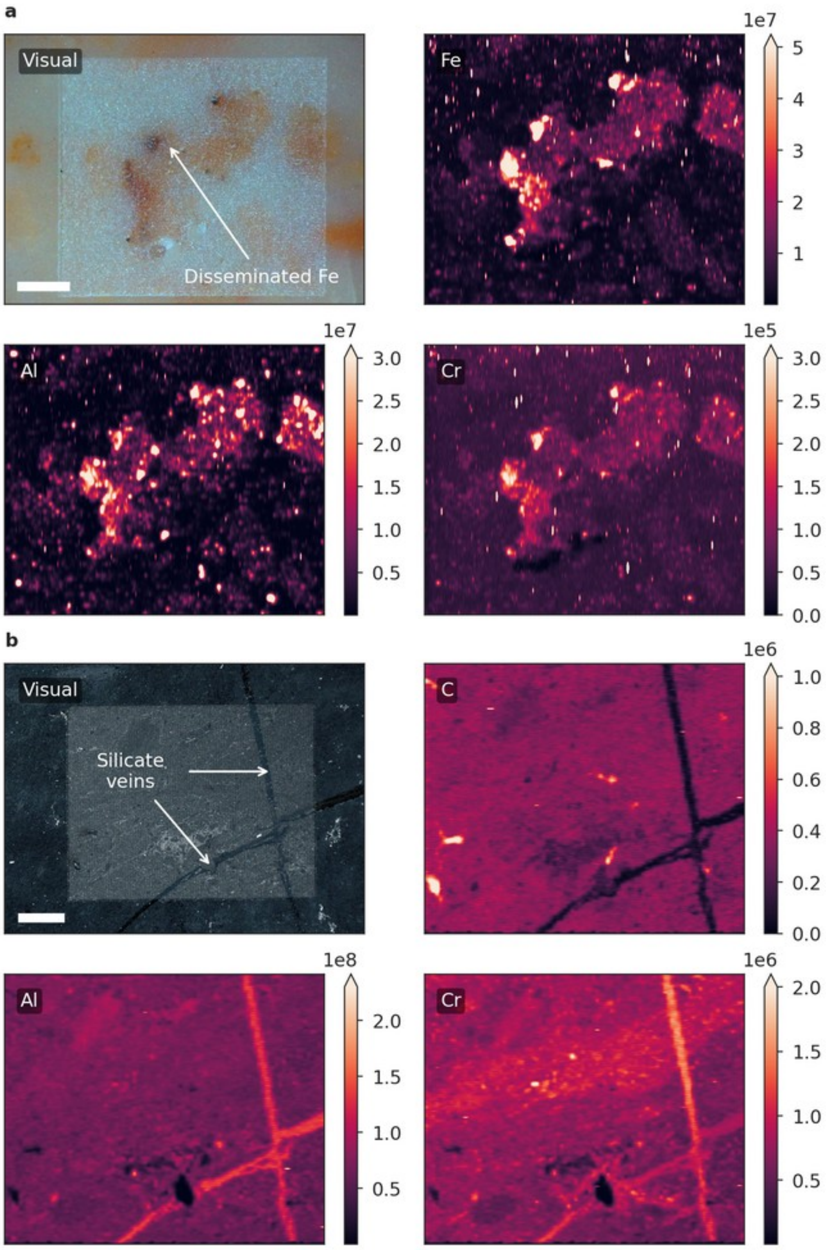
a
Visual
Disseminated Fe
Fe
1e7
5
4
3
2
1
Al
1e7
3.0
2.5
2.0
1.5
1.0
0.5
Cr
1e5
3.0
2.5
2.0
1.5
1.0
0.5
0.0
b
Visual
Silicate veins
C
1e6
1.0
0.8
0.6
0.4
0.2
0.0
Al
1e8
2.0
1.5
1.0
0.5
Cr
1e6
2.0
1.5
1.0
0.5

Figure 3:

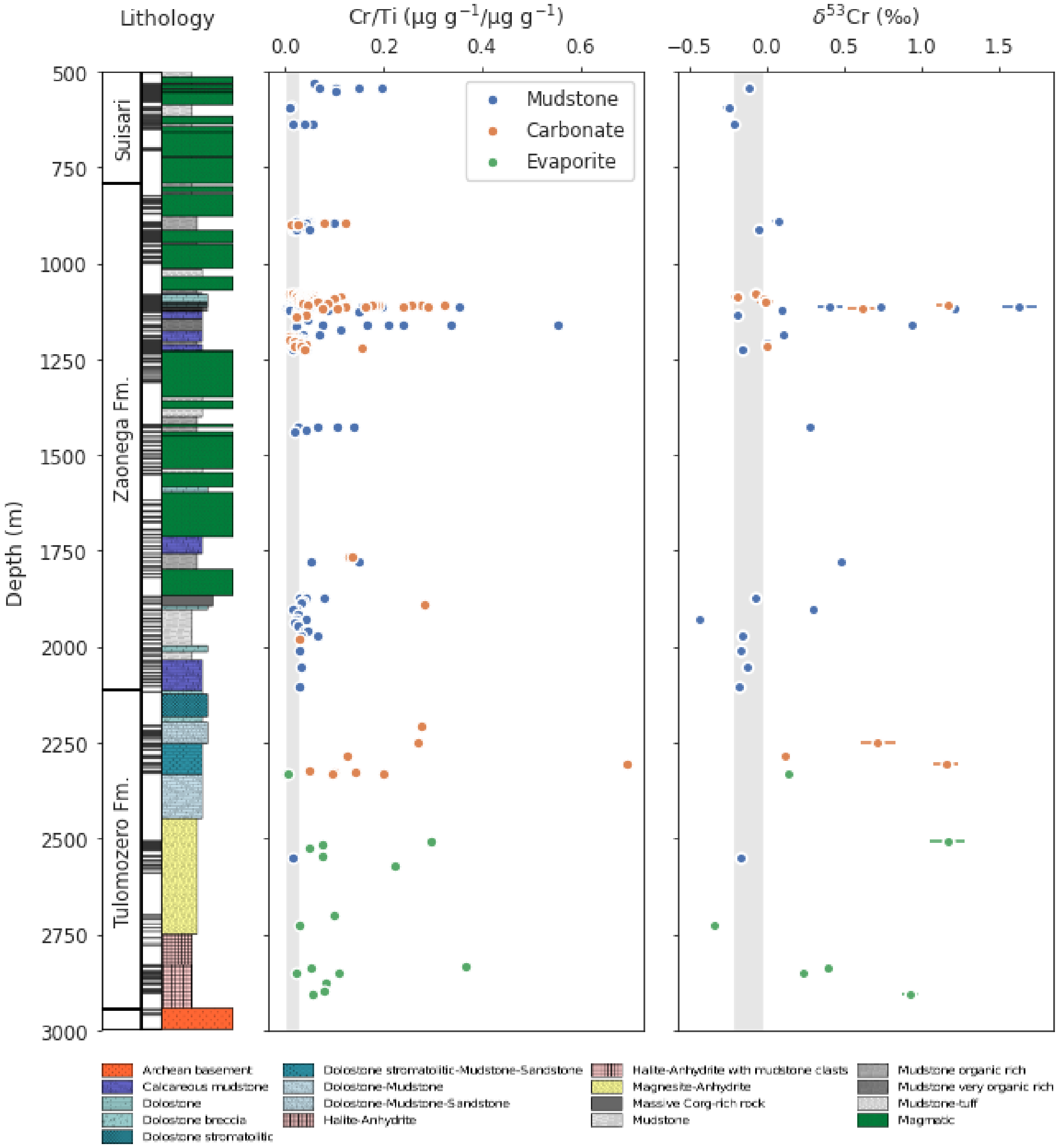
Lithology
Cr/Ti (µg g^{-1}/µg g^{-1})
δ^{53}Cr (‰)
0.0
0.2
0.4
0.6
−0.5
0.0
0.5
1.0
1.5
Depth (m)
500
750
1000
1250
1500
1750
2000
2250
2500
2750
3000
Suisari
Zaonega Fm.
Tulomozero Fm.
Mudstone
Carbonate
Evaporite
Archean basement
Calcareous mudstone
Dolostone
Dolostone breccia
Dolostone stromatolitic
Dolostone stromatolitic-Mudstone-Sandstone
Dolostone-Mudstone
Dolostone-Mudstone-Sandstone
Halite-Anhydrite
Halite-Anhydrite with mudstone clasts
Magnesite-Anhydrite
Massive Corg-rich rock
Mudstone
Mudstone organic rich
Mudstone very organic rich
Mudstone-tuff
Magmatic

Figure 4:

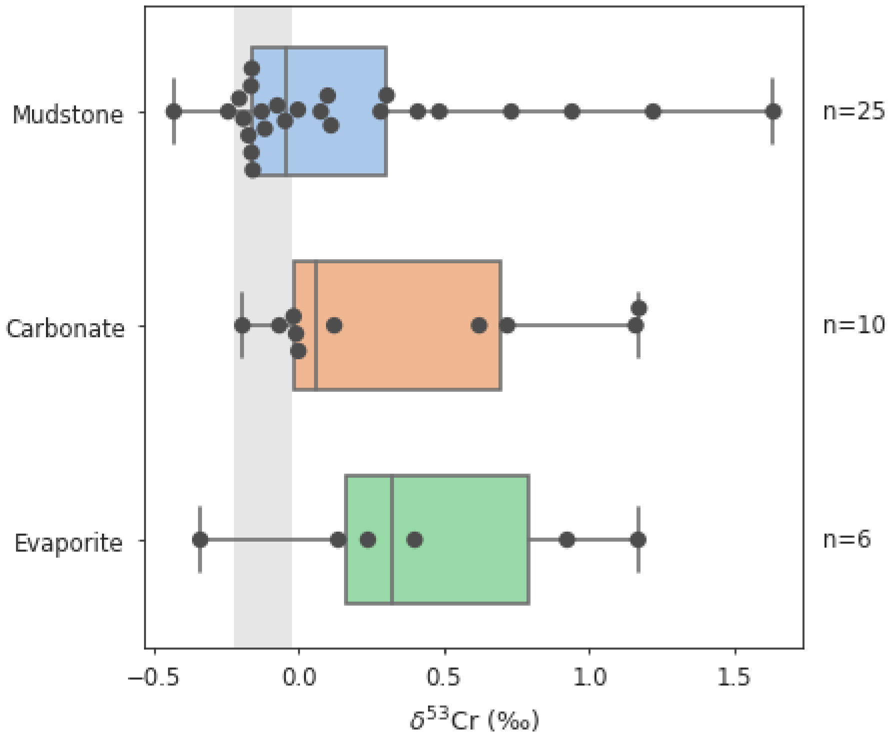
Mudstone
Carbonate
Evaporite
n=25
n=10
n=6
−0.5
0.0
0.5
1.0
1.5
δ^{53}Cr (‰)

Figure 5:

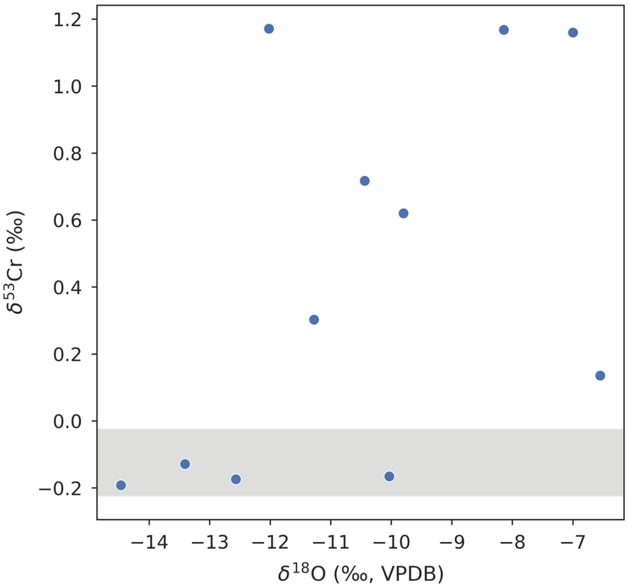
1.2
1.0
0.8
0.6
0.4
0.2
0.0
−0.2
δ^{53}Cr (‰)
−14
−13
−12
−11
−10
−9
−8
−7
δ^{18}O (‰, VPDB)

Figure 6:

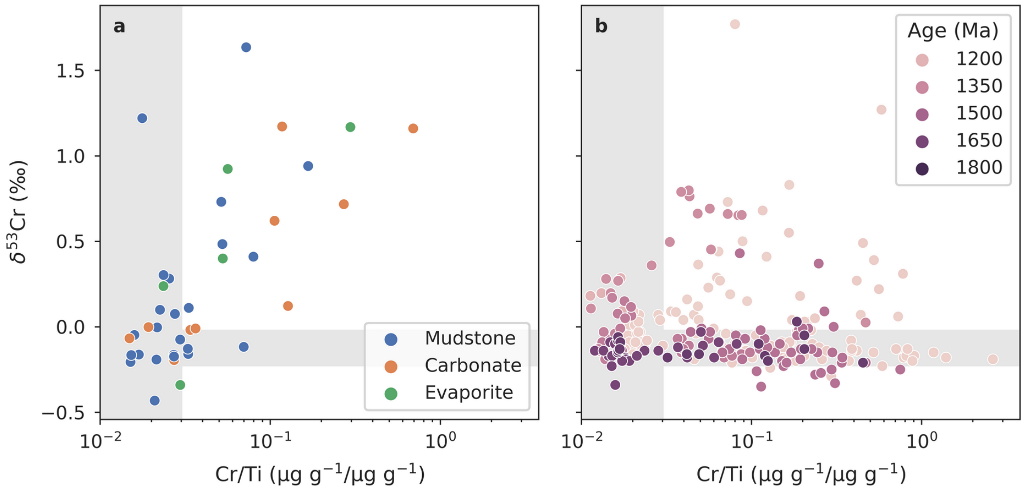
a
b
δ^{53}Cr (‰)
1.5
1.0
0.5
0.0
−0.5
10^{-2}
10^{-1}
10^{0}
Cr/Ti (µg g^{-1}/µg g^{-1})
● Mudstone
● Carbonate
● Evaporite
Age (Ma)
● 1200
● 1350
● 1500
● 1650
● 1800

Figure 7:

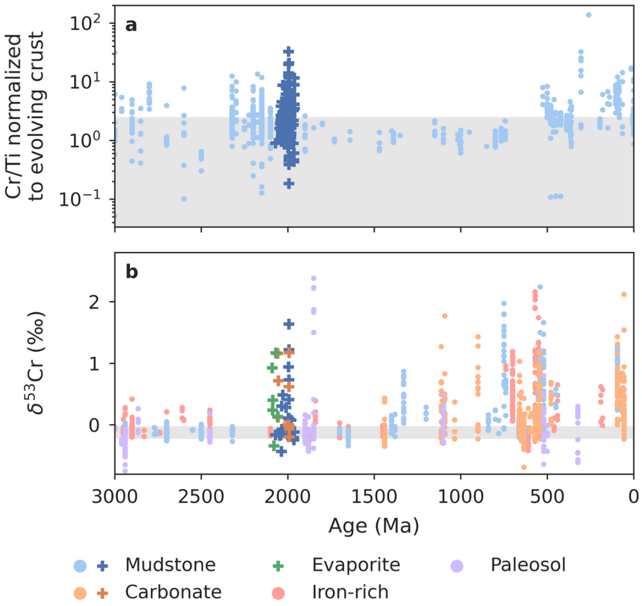
a
Cr/Ti normalized to evolving crust
10^2
10^1
10^0
10^{-1}
b
δ^{53}Cr (‰)
2
1
0
3000
2500
2000
1500
1000
500
0
Age (Ma)
Mudstone
Carbonate
Evaporite
Iron-rich
Paleosol

References

1. C. T. Reinhard, N. J. Planavsky, B. A. Ward, G. D. Love, G. L. Hir, A. Ridgwell, The impact of marine nutrient abundance on early eukaryotic ecosystems. *Geobiology*. **18**, 139–151 (2020).

2. D. B. Cole, D. B. Mills, D. H. Erwin, E. A. Sperling, S. M. Porter, C. T. Reinhard, N. J. Planavsky, On the co-evolution of surface oxygen levels and animals. *Geobiology*. **00**, 1–22 (2020).

3. J. L. Payne, A. G. Boyer, J. H. Brown, S. Finnegan, M. Kowalewski, R. A. Krause, S. K. Lyons, C. R. McClain, D. W. McShea, P. M. Novack-Gottshall, F. A. Smith, J. A. Stempien, S. C. Wang, Two-phase increase in the maximum size of life over 3.5 billion years reflects biological innovation and environmental opportunity. *Proc. Natl. Acad. Sci.* **106**, 24–27 (2009).

4. K. Zhang, X. Zhu, R. A. Wood, Y. Shi, Z. Gao, S. W. Poulton, Oxygenation of the Mesoproterozoic ocean and the evolution of complex eukaryotes. *Nat. Geosci.* **11**, 345–350 (2018).

5. R. A. Berner, J. M. VandenBrooks, P. D. Ward, Oxygen and Evolution. *Science*. **316**, 557–558 (2007).

6. D. C. Catling, C. R. Glein, K. J. Zahnle, C. P. McKay, Why O2 Is Required by Complex Life on Habitable Planets and the Concept of Planetary “Oxygenation Time.” *Astrobiology*. **5**, 415–438 (2005).

7. N. J. Butterfield, Oxygen, animals and oceanic ventilation: an alternative view. *Geobiology*. **7**, 1–7 (2009).

8. D. H. Erwin, Novelty and Innovation in the History of Life. *Curr. Biol.* **25**, R930–R940 (2015).

9. H. C. Betts, M. N. Puttick, J. W. Clark, T. A. Williams, P. C. J. Donoghue, D. Pisani, Integrated genomic and fossil evidence illuminates life’s early evolution and eukaryote origin. *Nat. Ecol. Evol.* **2**, 1556 (2018).

10. E. J. Javaux, K. Lepot, The Paleoproterozoic fossil record: Implications for the evolution of the biosphere during Earth’s middle-age. *Earth-Sci. Rev.* **176**, 68–86 (2018).

11. J. Farquhar, H. Bao, M. Thiemens, Atmospheric Influence of Earth’s Earliest Sulfur Cycle. *Science*. **289**, 756–758 (2000).

12. S. W. Poulton, A. Bekker, V. M. Cumming, A. L. Zerkle, D. E. Canfield, D. T. Johnston, A 200-million-year delay in permanent atmospheric oxygenation. *Nature*, 1–5 (2021).

13. M. R. Warke, T. D. Rocco, A. L. Zerkle, A. Lepland, A. R. Prave, A. P. Martin, Y. Ueno, D. J. Condon, M. W. Claire, The Great Oxidation Event preceded a Paleoproterozoic “snowball Earth.” *Proc. Natl. Acad. Sci.* **117**, 13314–13320 (2020).

14. H. Ohmoto, Y. Watanabe, A. C. Lasaga, H. Naraoka, I. Johnson, J. Brainard, A. Chorney, Oxygen, iron, and sulfur geochemical cycles on early Earth: Paradigms and contradictions (2014), doi:10.1130/2014.2504(09).

15. H. D. Holland, Volcanic gases, black smokers, and the great oxidation event. *Geochim. Cosmochim. Acta*. **66**, 3811–3826 (2002).

16. J. A. Karhu, H. D. Holland, Carbon isotopes and the rise of atmospheric oxygen. *Geology*. **24**, 867–870 (1996).

17. A. Bekker, H. D. Holland, Oxygen overshoot and recovery during the early Paleoproterozoic. *Earth Planet. Sci. Lett.* **317–318**, 295–304 (2012).

18. C. L. Blättler, M. W. Claire, A. R. Prave, K. Kirsimäe, J. A. Higgins, P. V. Medvedev, A. E. Romashkin, D. V. Rychanchik, A. L. Zerkle, K. Paiste, T. Kreitsmann, I. L. Millar, J. A. Hayles, H. Bao, A. V. Turchyn, M. R. Warke, A. Lepland, Two-billion-year-old evaporites capture Earth’s great oxidation. *Science*. **360**, 320–323 (2018).

19. N. J. Planavsky, A. Bekker, A. Hofmann, J. D. Owens, T. W. Lyons, Sulfur record of rising and falling marine oxygen and sulfate levels during the Lomagundi event. *Proc. Natl. Acad. Sci. U. S. A.* **109**, 18300–18305 (2012).

20. K. Mänd, S. V. Lalonde, L. J. Robbins, M. Thoby, K. Paiste, T. Kreitsmann, P. Paiste, C. T. Reinhard, A. E. Romashkin, N. J. Planavsky, K. Kirsimäe, A. Lepland, K. O. Konhauser, Palaeoproterozoic oxygenated oceans following the Lomagundi–Jatuli Event. *Nat. Geosci.* **13**, 302–306 (2020).

21. C. A. Partin, A. Bekker, N. J. Planavsky, C. T. Scott, B. C. Gill, C. Li, V. Podkovyrov, A. Maslov, K. O. Konhauser, S. V. Lalonde, G. D. Love, S. W. Poulton, T. W. Lyons, Large-scale fluctuations in Precambrian atmospheric and oceanic oxygen levels from the record of U in shales. *Earth Planet. Sci. Lett.* **369–370**, 284–293 (2013).

22. E. J. Bellefroid, A. v S. Hood, P. F. Hoffman, M. D. Thomas, C. T. Reinhard, N. J. Planavsky, Constraints on Paleoproterozoic atmospheric oxygen levels. *Proc. Natl. Acad. Sci. U. S. A.* **115**, 8104–8109 (2018).

23. D. Asael, F. L. H. Tissot, C. T. Reinhard, O. Rouxel, N. Dauphas, T. W. Lyons, E. Ponzevera, C. Liorzou, S. Chéron, Coupled molybdenum, iron and uranium stable isotopes as oceanic paleoredox proxies during the Paleoproterozoic Shunga Event. *Chem. Geol.* **362**, 193–210 (2013).

24. D. E. Canfield, L. Ngombi-Pemba, E. U. Hammarlund, S. Bengtson, M. Chaussidon, F. Gauthier-Lafaye, A. Meunier, A. Riboulleau, C. Rollion-Bard, O. Rouxel, D. Asael, A.-C. Pierson-Wickmann, A. El Albani, Oxygen dynamics in the aftermath of the

Great Oxidation of Earth’s atmosphere. *Proc. Natl. Acad. Sci. U. S. A.* **110**, 16736–16741 (2013).

25. F. Ossa Ossa, B. Eickmann, A. Hofmann, N. J. Planavsky, D. Asael, F. Pambo, A. Bekker, Two-step deoxygenation at the end of the Paleoproterozoic Lomagundi Event. *Earth Planet. Sci. Lett.* **486**, 70–83 (2018).

26. R. Frei, C. Gaucher, S. W. Poulton, D. E. Canfield, Fluctuations in Precambrian atmospheric oxygenation recorded by chromium isotopes. *Nature*. **461**, 250–253 (2009).

27. W. Wei, R. Klaebe, H.-F. Ling, F. Huang, R. Frei, Biogeochemical cycle of chromium isotopes at the modern Earth’s surface and its applications as a paleo-environment proxy. *Chem. Geol.* **541**, 119570 (2020).

28. M. Daye, V. Klepac-Ceraj, M. Pajusalu, S. Rowland, A. Farrell-Sherman, N. Beukes, N. Tamura, G. Fournier, T. Bosak, Light-driven anaerobic microbial oxidation of manganese. *Nature*. **576**, 311–314 (2019).

29. W. Liu, J. Hao, E. J. Elzinga, P. Piotrowiak, V. Nanda, N. Yee, P. G. Falkowski, Anoxic photogeochemical oxidation of manganese carbonate yields manganese oxide. *Proc. Natl. Acad. Sci.* **117**, 22698–22704 (2020).

30. D. B. Cole, C. T. Reinhard, X. Wang, B. Gueguen, G. P. Halverson, T. Gibson, M. S. W. Hodgskiss, N. R. McKenzie, T. W. Lyons, N. J. Planavsky, A shale-hosted Cr isotope record of low atmospheric oxygen during the Proterozoic. *Geology*. **44**, 555–558 (2016).

31. D. A. Colwyn, N. D. Sheldon, J. B. Maynard, R. Gaines, A. Hofmann, X. Wang, B. Gueguen, D. Asael, C. T. Reinhard, N. J. Planavsky, A paleosol record of the evolution of Cr redox cycling and evidence for an increase in atmospheric oxygen during the Neoproterozoic. *Geobiology*. **17**, 579–593 (2019).

32. N. J. Planavsky, C. T. Reinhard, X. Wang, D. Thomson, P. McGoldrick, R. H. Rainbird, T. Johnson, W. W. Fischer, T. W. Lyons, Low Mid-Proterozoic atmospheric oxygen levels and the delayed rise of animals. *Science*. **346**, 635–638 (2014).

33. D. E. Canfield, S. Zhang, A. B. Frank, X. Wang, H. Wang, J. Su, Y. Ye, R. Frei, Highly fractionated chromium isotopes in Mesoproterozoic-aged shales and atmospheric oxygen. *Nat. Commun.* **9**, 1–11 (2018).

34. G. J. Gilleaudeau, R. Frei, A. J. Kaufman, L. C. Kah, K. Azmy, J. K. Bartley, P. Chernyavskiy, A. H. Knoll, Oxygenation of the mid-Proterozoic atmosphere: clues from chromium isotopes in carbonates. *Geochem. Perspect. Lett.*, 178–187 (2016).

35. W. Wei, R. Frei, R. Klaebe, D. Tang, G.-Y. Wei, D. Li, L.-L. Tian, F. Huang, H.-F. Ling, A transient swing to higher oxygen levels in the atmosphere and oceans at ~1.4 Ga. *Precambrian Res.* **354**, 106058 (2021).

36. V. A. Melezhik, P. V. Medvedev, S. A. Svetov, in *Reading the Archive of Earth's Oxygenation*, V. A. Melezhik, A. R. Prave, A. E. Fallick, L. R. Kump, H. Strauss, A. Lepland, E. J. Hanski, Eds. (Springer, Berlin Heidelberg, 2013; http://link.springer.com/chapter/10.1007/978-3-642-29682-6_9), vol. 1: The Palaeoproterozoic of Fennoscandia As Context for the Fennoscandian Arctic Russia-Drilling Early Earth Project of *Frontiers in Earth Sciences*, pp. 387–490.

37. V. Krupenik, K. Sveshnikova, in *The Onega Palaeoproterozoic Structure (Geology, Tectonics, Deep Structure and Minerogeny)*, L. Glushanin, N. Sharov, V. Shchiptsov, Eds. (Institute of Geology, Karelian Research Centre of the Russian Academy of Sciences, 2011), pp. 190–195.

38. V. A. Melezhik, A. E. Fallick, P. V. Medvedev, V. V. Makarikhin, Extreme 13Ccarb enrichment in ca. 2.0 Ga magnesite–stromatolite–dolomite–`red beds' association in a global context: a case for the world-wide signal enhanced by a local environment. *Earth-Sci. Rev.* **48**, 71–120 (1999).

39. V. A. Melezhik, A. E. Fallick, M. M. Filippov, O. Larsen, Karelian shungite—an indication of 2.0-Ga-old metamorphosed oil-shale and generation of petroleum: geology, lithology and geochemistry. *Earth-Sci. Rev.* **47**, 1–40 (1999).

40. I. S. Puchtel, G. E. Brügmann, A. W. Hofmann, Precise Re–Os mineral isochron and Pb–Nd–Os isotope systematics of a mafic–ultramafic sill in the 2.0 Ga Onega plateau (Baltic Shield). *Earth Planet. Sci. Lett.* **170**, 447–461 (1999).

41. J. A. Karhu, *Paleoproterozoic evolution of the carbon isotope ratios of sedimentary carbonates in the Fennoscandian Shield* (Geologian tutkimuskeskus, Espoo, 1993), *Geological Survey of Finland Bulletin*.

42. M. Reuschel, V. A. Melezhik, M. J. Whitehouse, A. Lepland, A. E. Fallick, H. Strauss, Isotopic evidence for a sizeable seawater sulfate reservoir at 2.1 Ga. *Precambrian Res.* **192–195**, 78–88 (2012).

43. Y. Qu, A. E. Črne, A. Lepland, M. A. van Zuilen, Methanotrophy in a Paleoproterozoic oil field ecosystem, Zaonega Formation, Karelia, Russia. *Geobiology*. **10**, 467–78 (2012).

44. A. Lepland, L. Joosu, K. Kirsimäe, A. R. Prave, A. E. Romashkin, A. E. Črne, A. P. Martin, A. E. Fallick, P. Somelar, K. Üpraus, K. Mänd, N. M. W. Roberts, M. A. van Zuilen, R. Wirth, A. Schreiber, Potential influence of sulphur bacteria on Palaeoproterozoic phosphogenesis. *Nat. Geosci.* **7**, 20–24 (2014).

45. C. Scott, B. A. Wing, A. Bekker, N. J. Planavsky, P. Medvedev, S. M. Bates, M. Yun, T. W. Lyons, Pyrite multiple-sulfur isotope evidence for rapid expansion and contraction of the early Paleoproterozoic seawater sulfate reservoir. *Earth Planet. Sci. Lett.* **389**, 95–104 (2014).

46. K. Paiste, A. Lepland, A. L. Zerkle, K. Kirsimäe, G. Izon, N. K. Patel, F. McLean, T. Kreitsmann, K. Mänd, T. H. Bui, A. E. Romashkin, D. V. Rychanchik, A. R. Prave,

Multiple sulphur isotope records tracking basinal and global processes in the 1.98 Ga Zaonega Formation, NW Russia. *Chem. Geol.* **499**, 151–164 (2018).

47. K. Paiste, A. Pellerin, A. L. Zerkle, K. Kirsimäe, A. R. Prave, A. E. Romashkin, A. Lepland, The pyrite multiple sulfur isotope record of the 1.98 Ga Zaonega Formation: Evidence for biogeochemical sulfur cycling in a semi-restricted basin. *Earth Planet. Sci. Lett.* **534**, 116092 (2020).

48. V. A. Melezhik, A. E. Fallick, A. T. Brasier, A. Lepland, Carbonate deposition in the Palaeoproterozoic Onega basin from Fennoscandia: a spotlight on the transition from the Lomagundi-Jatuli to Shunga events. *Earth-Sci. Rev.* **147**, 65–98 (2015).

49. A. E. Črne, V. A. Melezhik, A. Lepland, A. E. Fallick, A. R. Prave, A. T. Brasier, Petrography and geochemistry of carbonate rocks of the Paleoproterozoic Zaonega Formation, Russia: Documentation of 13C-depleted non-primary calcite. *Precambrian Res.* **240**, 79–93 (2014).

50. T. Kreitsmann, M. Külaviir, A. Lepland, K. Paiste, P. Paiste, A. R. Prave, H. Sepp, A. E. Romashkin, D. V. Rychanchik, K. Kirsimäe, Hydrothermal dedolomitisation of carbonate rocks of the Paleoproterozoic Zaonega Formation, NW Russia — Implications for the preservation of primary C isotope signals. *Chem. Geol.* **512**, 43–57 (2019).

51. T. Kreitsmann, A. Lepland, M. Bau, A. Prave, K. Paiste, K. Mänd, H. Sepp, T. Martma, A. E. Romashkin, K. Kirsimäe, Oxygenated conditions in the aftermath of the Lomagundi-Jatuli Event: The carbon isotope and rare earth element signatures of the Paleoproterozoic Zaonega Formation, Russia. *Precambrian Res.* **347**, 105855 (2020).

52. L. R. Kump, C. Junium, M. A. Arthur, A. Brasier, A. Fallick, V. Melezhik, A. Lepland, A. E. Črne, G. Luo, Isotopic evidence for massive oxidation of organic matter following the Great Oxidation Event. *Science*. **334**, 1694–1696 (2011).

53. Yu. V. Amelin, L. M. Heaman, V. S. Semenov, U-Pb geochronology of layered mafic intrusions in the eastern Baltic Shield: implications for the timing and duration of Paleoproterozoic continental rifting. *Precambrian Res.* **75**, 31–46 (1995).

54. G. V. Ovchinnikova, a. B. Kuznetsov, V. A. Melezhik, I. M. Gorokhov, I. M. Vasil'eva, B. M. Gorokhovskii, Pb-Pb age of Jatulian carbonate rocks: The Tulomozero Formation of southeast Karelia. *Stratigr. Geol. Correl.* **15**, 359–372 (2007).

55. A. P. Martin, D. J. Condon, A. R. Prave, A. Lepland, A review of temporal constraints for the Palaeoproterozoic large, positive carbonate carbon isotope excursion (the Lomagundi–Jatuli Event). *Earth-Sci. Rev.* **127**, 242–261 (2013).

56. A. P. Martin, A. R. Prave, D. J. Condon, A. Lepland, A. E. Fallick, A. E. Romashkin, P. V. Medvedev, D. V. Rychanchik, Multiple Palaeoproterozoic carbon burial episodes and excursions. *Earth Planet. Sci. Lett.* **424**, 226–236 (2015).

57. I. S. Puchtel, N. T. Arndt, A. W. Hofmann, K. M. Haase, A. Kröner, V. S. Kulikov, V. V. Kulikova, C.-D. Garbe-Schönberg, A. A. Nemchin, Petrology of mafic lavas within the Onega plateau, central Karelia: evidence for 2.0 Ga plume-related continental crustal growth in the Baltic Shield. *Contrib. Mineral. Petrol.* **130**, 134–153 (1998).

58. N. Priyatkina, A. K. Khudoley, V. N. Ustinov, K. Kullerud, 1.92 Ga kimberlitic rocks from Kimozero, NW Russia: Their geochemistry, tectonic setting and unusual field occurrence. *Precambrian Res.* **249**, 162–179 (2014).

59. A. Stepanova, A. Samsonov, A. Larionov, The final episode of middle Proterozoic magmatism in the Onega structure: Data on trans-Onega dolerites. *Trans. Karelian Res. Cent. Russ. Acad. Sci. Precambrian Geol. Ser.* **1**, 3–16 (2014).

60. A. M. Bauer, A. D. Rooney, A. Lepland, D. B. Cole, N. J. Planavsky, in *Geobiology 2019 Conference Proceedings* (Banff, Canada, 2019; https://cms.eas.ualberta.ca/geobiology2019/wp-content/uploads/sites/28/2019/06/Geobiology-Conference-proceedings.pdf).

61. R. Schoenberg, S. Zink, M. Staubwasser, F. von Blanckenburg, The stable Cr isotope inventory of solid Earth reservoirs determined by double spike MC-ICP-MS. *Chem. Geol.* **249**, 294–306 (2008).

62. E. Schauble, G. R. Rossman, H. P. Taylor, Theoretical estimates of equilibrium chromium-isotope fractionations. *Chem. Geol.* **205**, 99–114 (2004).

63. M. Miletto, X. Wang, N. J. Planavsky, G. W. Luther, T. W. Lyons, B. M. Tebo, Marine microbial Mn(II) oxidation mediates Cr(III) oxidation and isotope fractionation. *Geochim. Cosmochim. Acta*. **297**, 101–119 (2021).

64. E. M. Saad, X. Wang, N. J. Planavsky, C. T. Reinhard, Y. Tang, Redox-independent chromium isotope fractionation induced by ligand-promoted dissolution. *Nat. Commun.* **8**, 1–10 (2017).

65. A. S. Ellis, T. M. Johnson, T. D. Bullen, Chromium Isotopes and the Fate of Hexavalent Chromium in the Environment. *Science*. **295**, 2060–2062 (2002).

66. K. Scheiderich, M. Amini, C. Holmden, R. Francois, Global variability of chromium isotopes in seawater demonstrated by Pacific, Atlantic, and Arctic Ocean samples. *Earth Planet. Sci. Lett.* **423**, 87–97 (2015).

67. C. T. Reinhard, N. J. Planavsky, L. J. Robbins, C. A. Partin, B. C. Gill, S. V. Lalonde, A. Bekker, K. O. Konhauser, T. W. Lyons, Proterozoic ocean redox and biogeochemical stasis. *Proc. Natl. Acad. Sci. U. S. A.* **110**, 5357–5362 (2013).

68. C. T. Reinhard, N. J. Planavsky, X. Wang, W. W. Fischer, T. M. Johnson, T. W. Lyons, The isotopic composition of authigenic chromium in anoxic marine sediments: A case study from the Cariaco Basin. *Earth Planet. Sci. Lett.* **407**, 9–18 (2014).

69. J. Farkaš, J. Frýda, C. Paulukat, E. C. Hathorne, Š. Matoušková, J. Rohovec, B. Frýdová, M. Francová, R. Frei, Chromium isotope fractionation between modern

seawater and biogenic carbonates from the Great Barrier Reef, Australia: Implications for the paleo-seawater δ53Cr reconstruction. *Earth Planet. Sci. Lett.* **498**, 140–151 (2018).

70. A. Rodler, N. Sánchez-Pastor, L. Fernández-Díaz, R. Frei, Fractionation behavior of chromium isotopes during coprecipitation with calcium carbonate: Implications for their use as paleoclimatic proxy. *Geochim. Cosmochim. Acta*. **164**, 221–235 (2015).

71. A. Pérez-Fodich, M. Reich, F. Álvarez, G. T. Snyder, R. Schoenberg, G. Vargas, Y. Muramatsu, U. Fehn, Climate change and tectonic uplift triggered the formation of the Atacama Desert's giant nitrate deposits. *Geology*. **42**, 251–254 (2014).

72. D. B. Cole, S. Zhang, N. J. Planavsky, A new estimate of detrital redox-sensitive metal concentrations and variability in fluxes to marine sediments. *Geochim. Cosmochim. Acta*. **215**, 337–353 (2017).

73. A. D. Anbar, H. D. Holland, The photochemistry of manganese and the origin of banded iron formations. *Geochim. Cosmochim. Acta*. **56**, 2595–2603 (1992).

74. A. A. Migdisov, X. Guo, A. E. Williams-Jones, C. J. Sun, O. Vasyukova, I. Sugiyama, S. Fuchs, K. Pearce, R. Roback, Hydrocarbons as ore fluids. *Geochem. Perspect. Lett.* **5**, 47–52 (2017).

75. Y. Gao, J. F. Casey, L. M. Bernardo, W. Yang, K. K. (Adry) Bissada, in *From Source to Seep: Geochemical Applications in Hydrocarbon Systems* (Geological Society of London, London, 2018; https://pubs.geoscienceworld.orghttps://pubs.geoscienceworld.org/books/book/2119/chapter/115206285/Vanadium-isotope-composition-of-crude-oil-effects), vol. 468.

76. G. T. Ventura, L. Gall, C. Siebert, J. Prytulak, P. Szatmari, M. Hürlimann, A. N. Halliday, The stable isotope composition of vanadium, nickel, and molybdenum in crude oils. *Appl. Geochem.* **59**, 104–117 (2015).

77. J. L. Banner, G. N. Hanson, Calculation of simultaneous isotopic and trace element variations during water-rock interaction with applications to carbonate diagenesis. *Geochim. Cosmochim. Acta*. **54**, 3123–3137 (1990).

78. R. Klaebe, P. Swart, R. Frei, Chromium isotope heterogeneity on a modern carbonate platform. *Chem. Geol.* **573**, 120227 (2021).

79. K. Mänd, S. V. Lalonde, K. Paiste, M. Thoby, K. Lumiste, L. J. Robbins, T. Kreitsmann, A. E. Romashkin, K. Kirsimäe, A. Lepland, K. O. Konhauser, Iron Isotopes Reveal a Benthic Iron Shuttle in the Palaeoproterozoic Zaonega Formation: Basinal Restriction, Euxinia, and the Effect on Global Palaeoredox Proxies. *Minerals*. **11**, 368 (2021).

80. K. Paiste, A. Lepland, A. L. Zerkle, K. Kirsimäe, T. Kreitsmann, K. Mänd, A. E. Romashkin, D. V. Rychanchik, A. R. Prave, Identifying global vs. basinal controls on

Paleoproterozoic organic carbon and sulfur isotope records. *Earth-Sci. Rev.* **207**, 103230 (2020).

81. D. Asael, O. Rouxel, S. W. Poulton, T. W. Lyons, A. Bekker, Molybdenum record from black shales indicates oscillating atmospheric oxygen levels in the early Paleoproterozoic. *Am. J. Sci.* **318**, 275–299 (2018).

82. D. S. Hardisty, Z. Lu, N. J. Planavsky, A. Bekker, P. Philippot, X. Zhou, T. W. Lyons, An iodine record of Paleoproterozoic surface ocean oxygenation. *Geology*. **42**, 619–622 (2014).

83. M. A. Kipp, E. E. Stüeken, A. Bekker, R. Buick, Selenium isotopes record extensive marine suboxia during the Great Oxidation Event. *Proc. Natl. Acad. Sci. U. S. A.* **114**, 875–880 (2017).

84. K. O. Konhauser, S. V. Lalonde, N. J. Planavsky, E. Pecoits, T. W. Lyons, S. J. Mojzsis, O. J. Rouxel, M. E. Barley, C. Rosìere, P. W. Fralick, L. R. Kump, A. Bekker, Aerobic bacterial pyrite oxidation and acid rock drainage during the Great Oxidation Event. *Nature*. **478**, 369–373 (2011).

85. L. J. Robbins, S. V. Lalonde, N. J. Planavsky, C. A. Partin, C. T. Reinhard, B. Kendall, C. Scott, D. S. Hardisty, B. C. Gill, D. S. Alessi, C. L. Dupont, M. A. Saito, S. A. Crowe, S. W. Poulton, A. Bekker, T. W. Lyons, K. O. Konhauser, Trace elements at the intersection of marine biological and geochemical evolution. *Earth-Sci. Rev.* **163**, 323–348 (2016).

86. K. Bakakas Mayika, M. Moussavou, A. R. Prave, A. Lepland, M. Mbina, K. Kirsimäe, The Paleoproterozoic Francevillian succession of Gabon and the Lomagundi-Jatuli event. *Geology* (2020), doi:10.1130/G47651.1.

87. P. Fralick, N. Planavsky, J. Burton, I. Jarvis, W. D. Addison, T. J. Barrett, G. R. Brumpton, Geochemistry of Paleoproterozoic Gunflint Formation carbonate: Implications for hydrosphere-atmosphere evolution. *Precambrian Res.* **290**, 126–146 (2017).

88. R. Frei, A. Polat, Chromium isotope fractionation during oxidative weathering—Implications from the study of a Paleoproterozoic (ca. 1.9Ga) paleosol, Schreiber Beach, Ontario, Canada. *Precambrian Res.* **224**, 434–453 (2013).

89. M. G. Babechuk, I. C. Kleinhanns, R. Schoenberg, Chromium geochemistry of the ca. 1.85 Ga Flin Flon paleosol. *Geobiology*. **15**, 30–50 (2017).

90. J. Toma, C. Holmden, P. Shakotko, Y. Pan, L. Ootes, Cr isotopic insights into ca. 1.9 Ga oxidative weathering of the continents using the Beaverlodge Lake paleosol, Northwest Territories, Canada. *Geobiology*. **17**, 467–489 (2019).

91. N. J. Planavsky, D. B. Cole, T. T. Isson, C. T. Reinhard, P. W. Crockford, N. D. Sheldon, T. W. Lyons, A case for low atmospheric oxygen levels during Earth's middle history. *Emerg. Top. Life Sci.* **2**, 149–159 (2018).

92. D. Tang, X. Shi, J. Ma, G. Jiang, X. Zhou, Q. Shi, Formation of shallow-water glaucony in weakly oxygenated Precambrian ocean: An example from the Mesoproterozoic Tieling Formation in North China. *Precambrian Res.* **294**, 214–229 (2017).

93. E. A. Sperling, C. A. Frieder, A. V. Raman, P. R. Girguis, L. A. Levin, A. H. Knoll, Oxygen, ecology, and the Cambrian radiation of animals. *Proc. Natl. Acad. Sci.* **110**, 13446–13451 (2013).

94. R. Tostevin, R. A. Wood, G. A. Shields, S. W. Poulton, R. Guilbaud, F. Bowyer, A. M. Penny, T. He, A. Curtis, K. H. Hoffmann, M. O. Clarkson, Low-oxygen waters limited habitable space for early animals. *Nat. Commun.* **7**, 12818 (2016).

95. N. J. Butterfield, Early evolution of the Eukaryota. *Palaeontology*. **58**, 5–17 (2015).

96. E. J. Javaux, A. H. Knoll, M. Walter, Recognizing and Interpreting the Fossils of Early Eukaryotes. *Orig. Life Evol. Biosph.* **33**, 75–94 (2003).

97. S. Zhu, M. Zhu, A. H. Knoll, Z. Yin, F. Zhao, S. Sun, Y. Qu, M. Shi, H. Liu, Decimetre-scale multicellular eukaryotes from the 1.56-billion-year-old Gaoyuzhuang Formation in North China. *Nat. Commun.* **7**, 11500 (2016).

98. H. Agić, M. Moczydłowska, L. Yin, Diversity of organic-walled microfossils from the early Mesoproterozoic Ruyang Group, North China Craton – A window into the early eukaryote evolution. *Precambrian Res.* **297**, 101–130 (2017).

99. E. J. Javaux, A. H. Knoll, M. R. Walter, TEM evidence for eukaryotic diversity in mid-Proterozoic oceans. *Geobiology*. **2**, 121–132 (2004).

100. D. M. Lamb, S. M. Awramik, D. J. Chapman, S. Zhu, Evidence for eukaryotic diversification in the ∼1800 million-year-old Changzhougou Formation, North China. *Precambrian Res.* **173**, 93–104 (2009).

101. L. Miao, M. Moczydłowska, S. Zhu, M. Zhu, New record of organic-walled, morphologically distinct microfossils from the late Paleoproterozoic Changcheng Group in the Yanshan Range, North China. *Precambrian Res.* **321**, 172–198 (2019).

102. B. Prasad, S. N. Uniyal, R. Asher, Organic-walled microfossils from the Proterozoic Vindhyan Supergroup of Son Valley, Madhya Pradesh, India. *Paleobotanist*. **54**, 13–60 (2005).

103. N. G. Vorob’eva, V. N. Sergeev, P. Yu. Petrov, Kotuikan Formation assemblage: A diverse organic-walled microbiota in the Mesoproterozoic Anabar succession, northern Siberia. *Precambrian Res.* **256**, 201–222 (2015).

104. T. W. Lyons, C. T. Reinhard, N. J. Planavsky, The rise of oxygen in Earth’s early ocean and atmosphere. *Nature*. **506**, 307–15 (2014).

105. V. A. Melezhik, A. R. Prave, E. J. Hanski, A. E. Fallick, A. Lepland, L. R. Kump, H. Strauss, Eds., *Reading the Archive of Earth’s Oxygenation* (Springer, Berlin

Heidelberg, 2013; http://link.springer.com/book/10.1007/978-3-642-29659-8), vol. 2: The Core Archive of the Fennoscandian Arctic Russia-Drilling Early Earth Project of *Frontiers in Earth Sciences*.

106. E. J. Javaux, K. Lepot, M. van Zuilen, V. A. Melezhik, P. V. Medvedev, in *Reading the Archive of Earth's Oxygenation*, V. A. Melezhik, A. R. Prave, A. E. Fallick, E. J. Hanski, A. Lepland, L. R. Kump, H. Strauss, Eds. (Springer, Berlin Heidelberg, 2013), vol. 3: Global Events and the Fennoscandian Arctic Russia-Drilling Early Earth Project of *Frontiers in Earth Sciences*, pp. 1352–1370.

107. C. R. Woltz, S. M. Porter, H. Agić, C. M. Dehler, C. K. Junium, L. A. Riedman, M. S. W. Hodgskiss, S. Wörndle, G. P. Halverson, Total organic carbon and the preservation of organic-walled microfossils in Precambrian shale. *Geology*. **49**, 556–560 (2021).

108. J. D. Schiffbauer, A. F. Wallace, J. L. Hunter, M. Kowalewski, R. J. Bodnar, S. Xiao, Thermally-induced structural and chemical alteration of organic-walled microfossils: an experimental approach to understanding fossil preservation in metasediments. *Geobiology*. **10**, 402–423 (2012).

109. A. El Albani, S. Bengtson, D. E. Canfield, A. Bekker, R. Macchiarelli, A. Mazurier, E. U. Hammarlund, P. Boulvais, J.-J. Dupuy, C. Fontaine, F. T. Fürsich, F. Gauthier-Lafaye, P. Janvier, E. Javaux, F. O. Ossa, A.-C. Pierson-Wickmann, A. Riboulleau, P. Sardini, D. Vachard, M. Whitehouse, A. Meunier, Large colonial organisms with coordinated growth in oxygenated environments 2.1 Gyr ago. *Nature*. **466**, 100–104 (2010).

110. A. El Albani, S. Bengtson, D. E. Canfield, A. Riboulleau, C. R. Bard, R. Macchiarelli, L. N. Pemba, E. Hammarlund, A. Meunier, I. M. Mouele, K. Benzerara, S. Bernard, P. Boulvais, M. Chaussidon, C. Cesari, C. Fontaine, E. Chi-Fru, J. M. G. Ruiz, F. Gauthier-Lafaye, A. Mazurier, A. C. Pierson-Wickmann, O. Rouxel, A. Trentesaux, M. Vecoli, G. J. M. Versteegh, L. White, M. Whitehouse, A. Bekker, The 2.1 Ga old Francevillian Biota: Biogenicity, taphonomy and biodiversity. *PLoS ONE*. **9**, e99438 (2014).

111. S. Bengtson, B. Rasmussen, M. Ivarsson, J. Muhling, C. Broman, F. Marone, M. Stampanoni, A. Bekker, Fungus-like mycelial fossils in 2.4-billion-year-old vesicular basalt. *Nat. Ecol. Evol.* **1**, 1–6 (2017).

112. A. El Albani, M. G. Mangano, L. A. Buatois, S. Bengtson, A. Riboulleau, A. Bekker, K. Konhauser, T. Lyons, C. Rollion-Bard, O. Bankole, S. G. L. Baghekema, A. Meunier, A. Trentesaux, A. Mazurier, J. Aubineau, C. Laforest, C. Fontaine, P. Recourt, E. C. Fru, R. Macchiarelli, J. Y. Reynaud, F. Gauthier-Lafaye, D. E. Canfield, Organism motility in an oxygenated shallow-marine environment 2.1 billion years ago. *Proc. Natl. Acad. Sci.* **116**, 3431–3436 (2019).

113. S. Bengtson, B. Rasmussen, B. Krapež, The Paleoproterozoic megascopic Stirling biota. *Paleobiology*. **33**, 351–381 (2007).

114. S. Bengtson, B. Rasmussen, New and Ancient Trace Makers. *Science*. **323**, 346–347 (2009).

115. R. P. Anderson, L. G. Tarhan, K. E. Cummings, N. J. Planavsky, M. Bjørnerud, Macroscopic structures in the 1.1 GA continental Copper Harbor Formation: Concretions or fossils? *Palaios*. **31**, 327–338 (2016).

116. S. McMahon, Earth's earliest and deepest purported fossils may be iron-mineralized chemical gardens. *Proc. R. Soc. B Biol. Sci.* **286**, 20192410 (2019).

117. K. P. Jochum, U. Nohl, K. Herwig, E. Lammel, B. Stoll, A. W. Hofmann, GeoReM: A New Geochemical Database for Reference Materials and Isotopic Standards. *Geostand. Geoanalytical Res.* **29**, 333–338 (2005).

118. J. Rosenbaum, S. M. F. Sheppard, An isotopic study of siderites, dolomites and ankerites at high temperatures. *Geochim. Cosmochim. Acta*. **50**, 1147–1150 (1986).

119. C. Siebert, T. F. Nägler, J. D. Kramers, Determination of molybdenum isotope fractionation by double-spike multicollector inductively coupled plasma mass spectrometry. *Geochem. Geophys. Geosystems*. **2**, 1032 (2001).

120. A. E. Črne, V. A. Melezhik, A. R. Prave, A. Lepland, A. E. Romashkin, D. V. Rychanchik, E. J. Hanski, Zh.-Y. Luo, in *Reading the Archive of Earth's Oxygenation*, V. A. Melezhik, A. R. Prave, A. E. Fallick, E. Hanski, A. Lepland, L. R. Kump, H. Strauss, Eds. (Springer, Berlin Heidelberg, 2013), vol. 2: The Core Archive of the Fennoscandian Arctic Russia-Drilling Early Earth Project of *Frontiers in Earth Sciences*, pp. 946–1007.

121. V. A. Melezhik, A. R. Prave, A. Lepland, A. E. Romashkin, D. V. Rychanchik, E. J. Hanski, in *Reading the Archive of Earth's Oxygenation*, V. A. Melezhik, A. R. Prave, A. E. Fallick, E. J. Hanski, A. Lepland, L. R. Kump, H. Strauss, Eds. (Springer, Berlin Heidelberg, 2013), vol. 2: The COre Archive of the Fennoscandian Arctic Russia-Drilling Early Earth Project of *Frontiers in Earth Sciences*, pp. 889–945.

122. K. C. Condie, Chemical composition and evolution of the upper continental crust: Contrasting results from surface samples and shales. *Chem. Geol.* **104**, 1–37 (1993).

123. J. H. Jamieson-Hanes, B. D. Gibson, M. B. J. Lindsay, Y. Kim, C. J. Ptacek, D. W. Blowes, Chromium Isotope Fractionation During Reduction of Cr(VI) Under Saturated Flow Conditions. *Environ. Sci. Technol.* **46**, 6783–6789 (2012).

124. D. M. Semeniuk, M. T. Maldonado, S. L. Jaccard, Chromium uptake and adsorption in marine phytoplankton – Implications for the marine chromium cycle. *Geochim. Cosmochim. Acta*. **184**, 41–54 (2016).

125. A. B. Frank, R. M. Klaebe, S. Löhr, L. Xu, R. Frei, Chromium isotope composition of organic-rich marine sediments and their mineral phases and implications for using black shales as a paleoredox archive. *Geochim. Cosmochim. Acta*. **270**, 338–359 (2020).

126. C. Kim, Q. Zhou, B. Deng, E. C. Thornton, H. Xu, Chromium(VI) Reduction by Hydrogen Sulfide in Aqueous Media: Stoichiometry and Kinetics. *Environ. Sci. Technol.* **35**, 2219–2225 (2001).

127. J. E. Johnson, S. M. Webb, K. Thomas, S. Ono, J. L. Kirschvink, W. W. Fischer, Manganese-oxidizing photosynthesis before the rise of cyanobacteria. *Proc. Natl. Acad. Sci.* **110**, 11238–11243 (2013).

128. W. F. Martin, S. Garg, V. Zimorski, Endosymbiotic theories for eukaryote origin. *Philos. Trans. R. Soc. B Biol. Sci.* **370**, 20140330 (2015).

Supplementary material

Supplementary Figure 1

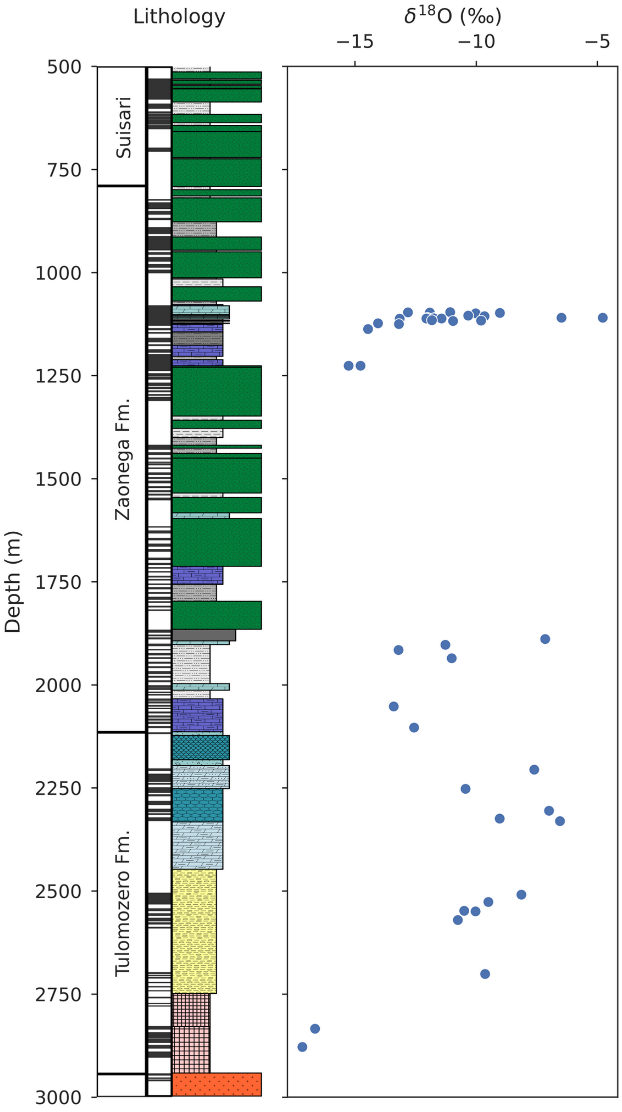

Figure S1: Carbonate oxygen isotope ratios (δ^{18}O VPDB) in the OPH drill core.

Supplementary Text

X-ray diffraction results

The Tulomozero Formation samples in the OPH drill core are dominated by halite below ~2800 m core depth (averaging 49.2±31.7 wt.%; reported as 1σ), with abundant magnesite and anhydrite (11.9±12.1 wt.% and 26.2±23.3 wt.%, respectively), and accessory evaporite minerals like hexahydrite, pentahydrite, starkeyite, kieserite, bloedite, leonite, langbeinite, kainite, and picomerite (all below 10 wt.%). Quartz is relatively common (averaging 10.4±10.0 wt.%), whereas other detrital minerals (e.g., K-feldspar, chlorite, hematite), talc, and dolomite are all present below 7.2 wt.%. From ~2800 to ~2330 m, halite gives way to evaporitic magnesite and anhydrite (averaging 44.6±28.2 wt.% and 25.9±18.9 wt.%, respectively), with major inputs of glauberite (5.5±15.6 wt.%), gypsum (2.0±4.0 wt.%), quartz (8.2±8.2 wt.%), and dolomite (3.6±11.4 wt.%) and an increased prevalence of aluminosilicates like plagioclase (up to 20.1 wt.%), K-feldspar, micas, and chlorite. From ~2330 m depth in the upper Tulomozero Formation to ~2100 m depth in the lower Zaonega Formation, the major mineral is dolomite (averaging 56.9±29.9 wt.%) with abundant magnesite interbeds (up to 68.1 wt.%), occasional quartz-feldspar-mica-chlorite-hematite layers (which contain up to ~30 wt.% of quartz and plagioclase), and accessory talc (below 3.0 wt.%). From ~2100 to 1700 m the mineralogy is similar, but quartz (averaging 16.1±8.9 wt.%) and aluminosilicates (25.5±23.4 wt.% plagioclase, 20.8±15.5 wt.% micas) tend to dominate over dolomite (17.4±26.2 wt.%). The sedimentary interval from 1230 to 1080 m is dominated by alternating dolomite-calcite (averaging 34.6±39.2 wt.% and 11.5±18.5 wt.%, respectively) and quartz-aluminosilicate assemblages (12.9±17.7 wt.% quartz, 15.7±18.2 wt.% micas, and 9.5±11.6 wt.% K-feldspar), the latter being more prevalent below 1112 m and the former above 1112 m. In this interval, pyrite and apatite are also common (3.8±5.2 wt.%, and 0.3±0.9 wt.%, respectively), especially near the 1112 m boundary. Sedimentary layers above this section, at 980–913 m, ~635 m, and ~590–530 m, contain mostly quartz, K-feldspar, plagioclase, and chlorite (averaging 23.7±20.1, 7.5±4.4, 30.1±16.3, and 20.6±18.0 wt.%, respectively).

Other processes that may affect Cr isotope ratios

Variation in sedimentary δ^{53}Cr can be explained through a variety of processes, the first of which is local post-depositional mobilization of Cr by hydrothermal fluids, as discussed in the main text. Alternatively, negative fractionations have been observed in Cr adsorption onto organic matter (e.g., *123*, *124*); the expression of isotope fractionation in sediments can then be modulated through a variable mixing relationship between different Cr hosting phases, or by diagenetic redistribution of Cr (*125*). Furthermore, the Zaonega Formation was characterized by highly variable redox conditions (*20*, *44*, *46*), which may also induce δ^{53}Cr variation: while Cr drawdown in anoxic waters is close to quantitative (*126*), in suboxic conditions the locus of reduction shifts into the sediments, so that a distilled, positively-fractionated Cr(VI) phase can escape back into the water column, leaving the sediments depleted in ^{53}Cr (*68*). Finally, the highly biologically productive local ecosystem in the Zaonega Formation (*43*, *44*, *47*) may, too, have induced δ^{53}Cr variability in the water column, as the photobiochemical reduction of Cr results in substantial δ^{53}Cr variation in oceanic depth gradients (*66*). However, all these processes require first that Cr(VI) be present—the implication being that oxidative weathering of Cr on land is a requisite.

Significantly, several recent studies have found alternative pathways of Mn oxidation and Cr fractionation that do not require the presence of free O_2. For example, Liu et al. (*29*) described anoxic and abiotic oxidation of Mn(II) carbonates (rhodochrosite) which can take place under UV radiation, producing Mn(III)-oxides which could, in turn, potentially drive Cr-isotope fractionation. Similarly, Daye et al. (*28*) reported anoxygenic photosynthetic organisms capable of oxidizing Mn(II) to Mn(III) and Mn(IV) without the presence of oxygen (see also *127*). Finally, Saad et al. (*64*) showed that ligand-based solubilization of Cr(III) can produce isotope fractionations of a magnitude and direction that are difficult to predict.

Although UV-dependent Mn oxidation is potentially relevant for the Archean, deposition of the Tulomozero and Zaonega rocks postdates the disappearance of sulfur mass-independent fractionation (and the formation of a UV-shielding ozone layer) by at least 200 Myr (*13*, *128*). Further, the abundance of authigenic Cr accumulation in the Zaonega Formation is most easily explained through a large dissolved marine Cr(VI) pool, which requires vigorous Cr solubilization on land, its riverine transfer into oceans, and the presence of oxic settings in the oceans so that Cr(VI) could accumulate. All of this is consistent with other proxy records in the Paleoproterozoic, which purport a fundamentally oxidized surface world (e.g., *17, 18, 21, 82*). Conversely, it is still unclear whether the relatively lower rates of ligand-based, non-redox Cr(III) solubilization can account for the necessary Cr fluxes (*64*), or whether likely short-lived Mn oxides generated through photochemical or photosynthetic processes on the surface in light-replete conditions are capable of affecting Cr oxidation at scale (*73*). Fundamentally, while all of these alternative processes are expected to have been in operation since the Archean, the highly fractionated Cr record in the Onega Basin is vastly different from anything in the Archean or early Mesoproterozoic. We contend, therefore, that O_2-driven Mn(IV) oxide generation remains the best explanation for the Onega Basin data (*26, 27*).